Available online at www.sciencedirect.com
ScienceDirect
Comput. Methods Appl. Mech. Engrg. 305 (2016) 62–88
Computer methods in applied mechanics and engineering
www.elsevier.com/locate/cma

Topology optimization with local stress constraint based on level set evolution via reaction–diffusion

Hélio Emmendoerfer Jr., Eduardo Alberto Fancello*

Department of Mechanical Engineering, Universidade Federal de Santa Catarina, Campus Universitário - Trindade, 88040-900, Florianópolis, SC, Brazil

Received 1 July 2015; received in revised form 16 February 2016; accepted 17 February 2016
Available online 2 March 2016

Abstract

This work focuses the structural topology optimization problem of mass minimization subject to local stress constraints. To this aim, two related issues are addressed. The first one is the successful strategy used to define local stress constraints by means of an Augmented Lagrangian approach. The second, and main contribution of the present paper, is the use of a reaction–diffusion equation to guide, via evolution of a level set, the design optimization sequence. The advantages of this strategy are twofold: firstly, it allows the creation of new holes during the optimization process, a significant feature for a true topological optimization method. Secondly, reinitialization steps usually found in classical Hamilton–Jacobi based evolution are eliminated with a significant improvement in convergence ease. A set of benchmark examples in two dimensions are presented. Numerical results show the efficiency of the algorithm to create new holes, identify stress concentrations and to provide stable optimization sequences converging to local minima defined by stress saturated designs.

Keywords: Topology optimization; Level sets; Stress constraints; Augmented Lagrangian; Reaction–diffusion equation

1. Introduction

Although the strain energy or total potential energy (compliance problem) has been the most widely used objective function in structural topology optimization due to their particularly convenient mathematical properties, the corresponding optimal designs are not validated against mechanical failure. Such designs need to be post processed and, after stress analysis verification, conveniently modified in order to satisfy some material failure criterion. With the aim to eliminate this necessary "rework", and despite challenging mathematical and numerical difficulties, stress-constrained topology optimization problems have attracted the attention of many researchers.

After the pioneering paper of Duysinx and Bendsøe [1] dealing with stress constraints in continuum structures, several studies have been published on this subject, most of them within the last decade. One of the first difficulties associated to this problem is the usually large number of stress constraints, direct consequence of their local nature.

* Corresponding author.
E-mail addresses: helio.e.j@posgrad.ufsc.br (H. Emmendoerfer Jr.), eduardo.fancello@ufsc.br (E.A. Fancello).

http://dx.doi.org/10.1016/j.cma.2016.02.024
0045-7825/

Aiming to tackle this issue, in [2] local constraints are treated using an Augmented Lagrangian approach combined with SIMP concepts. This approach was later extended to multiple load cases [3] and contact boundary conditions [4]. A different strategy followed by several works (see, for example, [5,6]) is to use integral forms of stress constraints based on p-norms or on the Kreisselmeier–Steinhauser (KS) function. Unfortunately, although this choice allows for a decrease of computational costs, the corresponding results are sometimes unable to account for stress concentrations. In an attempt to overcome this difficulty, different studies propose localization strategies in which a finite number of constraints are defined as integrals over subregions within the domain [7–13].

Another classical issue associated to stress constraints are the singular optima on the design space, undesirable outcome of topology approaches based on intermediate densities. Two main strategies are seen in the literature to deal with this problem. The first is the so-called ϵ-relaxed approach of Cheng and Guo [14]. The second, attributed to Bruggi [15,16] is called qp-approach. A comparative analysis of different propositions for stress-driven topology designs based on intermediate materials can be found in [8].

Stress based works considering failure criterion other than von Mises are seen in [17–19] where materials with different behavior in tension and compression are discussed. Similarly, constraints based on fatigue failure are considered in [20].

Concerning the topology optimization technique itself, formulations using implicit functions for design control have gained popularity. In [21], the topology optimization problem is formulated using an implicit function controlled by nodal variables. The papers of Allaire et al. [22] and Wang et al. [23] are considered the first ones combining an evolution equation for the level set with the sensitivity analysis of a cost function for structural topology optimization. For an overview of different level set techniques for topology optimization, the reader may see [24] and [25]. It is worth mentioning that all cited works refer to compliance problems.

Propositions relating level set with stress driven problems are seen in [26,27] (for stress minimization) and [28–31] (for stress constrained problems). The phase-field method has also been tested in [32,33]. An important different approach is found in works [19,34] where a simple algorithm based on topological derivative information provide excellent results for the local stress constrained problem.

Finally, we call attention to the recent paper [35]. Strongly related to the present work, the referred paper includes local stress constraints into the optimization problem via Augmented Lagrangian approach while the design is modified by a level set that moves by time integration of Hamilton–Jacobi equations. A well known drawback of this conventional evolution scheme is the inability of creating new holes [36]. Consequently, these approaches are sometimes called not topology but shape optimization techniques. Among different alternatives to overcome this limitation it is worth mentioning the work [27], where hole nucleation steps based on the information of topological derivatives are included, [37] using radial basis functions, [38] using evolutionary structural optimization and [39] considering a secondary level set function.

An interesting approach proposed by Yamada and co-workers [40,41] regularizes the optimization problem by introducing a reaction–diffusion equation for the evolution of the level set. This proposition avoids the undesirable reinitialization procedure classically needed with Hamilton–Jacobi evolution and also allows for the generation of new holes. The method was applied for compliance, compliant mechanisms, and eigenfrequency problems.

The purpose of present work is to reformulate the problem of minimum mass with stress constraints keeping the same successful local approach for stresses proposed in [35] but to modify the level set updating procedure. In [35] the level set is updated following an upwind time integration of the classical Hamilton–Jacobi equation. Despite the very satisfactory results obtained, the creation of new holes was not allowed and the final topology was quite influenced by the initial level set domain. In addition, reinitialization techniques were needed to control the shape of the level set function during the optimization procedure. The main reason behind the choice of a level-set approach to handle the stress constrained problem is the expectation that it may attenuate the mathematical/numerical difficulty known as singularity-stress (singular optima in the design space [14]) since the level-set field allows for a clear separation between material and void regions within the background domain.

In the present work the level set is updated based on a reaction–diffusion equation similar to that proposed in [40]. Two important consequences of this choice are achieved. The first is the elimination of a reinitialization step, source of noise in the solution near convergence. The second is the possibility of creation of new holes, allowing the optimization sequence to start for different configurations, even with no holes at all.

The subsequent text is organized as follows. Section 2 sets the optimization problem based on the same reasoning presented in [35] with a conveniently modified objective function. Section 3 describes the reaction–diffusion problem

that guides the level set evolution and corresponding minimizing sequence. The velocity field responsible for the decrease of the objective function is deduced in this section by means of sensitivity analysis. Numerical aspects and numerical examples are discussed in Sections 4 and 5, respectively. Final remarks are highlighted in Section 6.

2. Formulation of the problem

2.1. Basic statement

Let Ω be an open domain in $\mathbb{R}^n$ ($n = 2, 3$) occupied by a linear elastic isotropic body $\mathcal{B}$ with a smooth boundary $\partial\Omega = \Gamma_D \cup \Gamma_H \cup \Gamma_N$. Dirichlet boundary conditions are applied in Γ_D, while Γ_H is submitted to homogeneous Neumann conditions. Non-zero surface tractions $\boldsymbol{\tau}$ act on Γ_N. Boundary Γ_H may change during the optimization procedure, while Γ_D and Γ_N are assumed fixed. All admissible configurations Ω are defined within a fixed background domain D (Fig. 1). Body $\mathcal{B}$ is in equilibrium whenever the displacement field $\mathbf{u} \in U$ satisfies the integral equation

$$a(\mathbf{u}, \mathbf{v}) = l(\mathbf{v}) \quad \forall \mathbf{v} \in V. \tag{1}$$

Linear operators $a(\cdot, \cdot)$ and $l(\cdot)$ represent the virtual work of internal and external forces, respectively:

$$a(\mathbf{u}, \mathbf{v}) = \int_\Omega \mathbf{C}\boldsymbol{\varepsilon}(\mathbf{u}) \cdot \boldsymbol{\varepsilon}(\mathbf{v})\, d\Omega, \qquad l(\mathbf{v}) = \int_{\Gamma_N} \boldsymbol{\tau} \cdot \mathbf{v}\, d\partial\Omega, \tag{2}$$

while U and V are the sets of kinematically admissible displacements and admissible variations, respectively. $\boldsymbol{\varepsilon}(\mathbf{u}) = \nabla^s \mathbf{u}$ is the linear strain tensor and $\mathbf{C}$ is the isotropic elasticity tensor. For simplicity reasons, no body forces are considered in (2). Moreover, since U is a translation of the space V, the problem may be rewritten for simplicity reasons in such a way that $\mathbf{u} \in V$ modifying the term $l(\mathbf{v})$ conveniently.

The problem of minimum mass with local stress (failure) constraints is stated as:

Problem P_1:

$$\begin{aligned} &\min_{\Omega} \quad m(\mathbf{u}) = \int_\Omega \rho d\Omega + \mu \int_\Omega \frac{1}{2}\mathbf{C}\boldsymbol{\varepsilon}(\mathbf{u}) \cdot \boldsymbol{\varepsilon}(\mathbf{u}) d\Omega, \\ &\text{subject to: } \begin{cases} a_\Omega(\mathbf{u}, \mathbf{v}) - l_\Omega(\mathbf{v}) = 0, & \forall \mathbf{v} \in V, \\ g(\mathbf{u}) \le 0, & \forall \mathbf{x} \in \Omega, \end{cases} \end{aligned} \tag{3}$$

where ρ is the material density and $g(\mathbf{u})$ is a stress constraint that must be satisfied everywhere in Ω. The second term of the objective functional corresponds to the compliance (strain energy), which $\mu \ge 0$ is a weighting factor. As observed in [28], "the compliance term is introduced into the objective function in order to play the role of excluding the pathological structures with small stiffness from the feasible domain". Moreover, considering the present problem, mass is insensitive to the place where the material is removed and the compliance term also provides a preference direction on the sensitivity analysis. The weighting factor μ also plays the role of scaling factor since units of energy and mass are different.

2.2. Level set-based formulation

The level set approach relates the boundary $\partial\Omega$ with the zero-valued level set of a function $\phi : D \to \mathbb{R}$:

$$\phi(\mathbf{x}) > 0 \quad \forall \mathbf{x} \in \Omega, \tag{4}$$

$$\phi(\mathbf{x}) = 0 \quad \forall \mathbf{x} \in \partial\Omega, \tag{5}$$

$$\phi(\mathbf{x}) < 0 \quad \forall \mathbf{x} \in D \backslash (\Omega \cup \partial\Omega). \tag{6}$$

Accordingly to expressions (4)–(6), variations of ϕ modify the corresponding level sets and consequently the position of the boundary $\partial\Omega$ [36,42]. Using the Heaviside function

$$H(\phi(\mathbf{x})) = \begin{cases} 1, & \text{if } \phi(\mathbf{x}) \ge 0, \\ 0, & \text{if } \phi(\mathbf{x}) < 0, \end{cases} \tag{7}$$

Problem P_1 may be reformulated as an integral over a fixed domain D (also known as background domain) within which subdomain Ω evolves guided by the function ϕ:

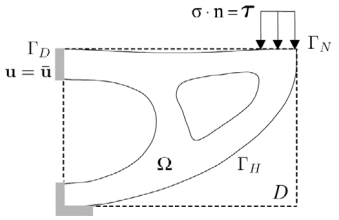

Fig. 1. Geometric definitions of a domain composed of solid and voids.

Problem P_2:

$$\min_{\phi} \quad m_\phi(\mathbf{u}) = \int_D \left[\rho(\phi) + \frac{\mu}{2}\mathbf{C}(\phi)\boldsymbol{\varepsilon}(\mathbf{u})\cdot\boldsymbol{\varepsilon}(\mathbf{u})\right] dD,$$
$$\text{subject to: } \begin{cases} a_\phi(\mathbf{u},\mathbf{v}) = l_\phi(\mathbf{v}), & \forall \mathbf{v} \in V, \\ H(\phi)g(\mathbf{u}) \le 0, & \forall \mathbf{x} \in D, \end{cases} \tag{8}$$

where

$$a_\phi(\mathbf{u},\mathbf{v}) = \int_D \mathbf{C}(\phi)\boldsymbol{\varepsilon}(\mathbf{u})\cdot\boldsymbol{\varepsilon}(\mathbf{v}) dD, \tag{9}$$

$$l_\phi(\mathbf{v}) = \int_{\Gamma_N} \boldsymbol{\tau}\cdot\mathbf{v} d\partial\Omega, \tag{10}$$

$$\rho(\phi) = H(\phi)\rho_1 + (1 - H(\phi))\rho_2, \tag{11}$$

$$\mathbf{C}(\phi) = H(\phi)^p\mathbf{C}_1 + (1 - H(\phi)^p)\mathbf{C}_2. \tag{12}$$

Eqs. (11) and (12) define the dependence of fields ρ and $\mathbf{C}$ on two material phases: $(\rho_1, \mathbf{C}_1)$ occupying domain Ω and $(\rho_2, \mathbf{C}_2)$ occupying the complement $D\backslash(\Omega \cup \partial\Omega)$. In the present case, properties of material 2 are significantly lower than those of material 1, that is, $\rho_2 \ll \rho_1$ and $\|\mathbf{C}_2\| \ll \|\mathbf{C}_1\|$. The reasons for the inclusion of an exponent $p > 1$ in Eq. (12) are twofold: Firstly, although exponent p has no effect on the exact Heaviside function (7), its use on a discretized counterpart of $\mathbf{C}(\phi)$, detailed in next section, will lead to the classical "ersatz" material model [22,23,43] for those elements cut by the implicit boundary $\partial\Omega$. Secondly, it plays a formal role in the derivative of $\mathbf{C}(\phi)$ with respect to function ϕ, explained in Section 3.1.

2.3. Equilibrium equation

The finite element counterpart of expressions (8) involves the integration over all elements defined in D, many of them cut by $\partial\Omega$. All these elements contain materials 1 and 2 simultaneously. Different works propose ways of conforming boundary and mesh by means of remeshing [44] or by using discontinuous X-FEM [26,29]. In the present work cut elements are preserved at the cost of addressing two technical questions: (a) computation of integrals $m_\phi(\mathbf{u})$ and $a_\phi(\mathbf{u},\mathbf{v})$; and (b) appropriate definition of stress constraint on these elements.

To address the first issue, integrals involving $\mathbf{C}(\phi)$ are approximated by a representative constant value $\mathbf{C}^e(\phi)$ over the element:

$$\begin{aligned} a_\phi(\mathbf{u},\mathbf{v}) &= \sum_{e=1}^{Nel}\int_{D_e} \mathbf{C}(\phi)\boldsymbol{\varepsilon}(\mathbf{u})\cdot\boldsymbol{\varepsilon}(\mathbf{v}) dD \\ &\approx \sum_{e=1}^{Nel}\int_{D_e} \mathbf{C}^e(\phi)\boldsymbol{\varepsilon}(\mathbf{u})\cdot\boldsymbol{\varepsilon}(\mathbf{v}) dD, \end{aligned} \tag{13}$$

$$\mathbf{C}^e(\phi) = a^e(\phi)^p\mathbf{C}_1 + \left[1 - a^e(\phi)^p\right]\mathbf{C}_2, \qquad a^e(\phi) = \frac{\int_{D_e} H(\phi) dD}{\int_{D_e} dD}, \tag{14}$$

where $a^e(\phi)$ is the area fraction of element e covered by material 1. It is worth noting that this expression is nothing but the classical "ersatz" material model, significant only for elements cut by $\partial\Omega$.

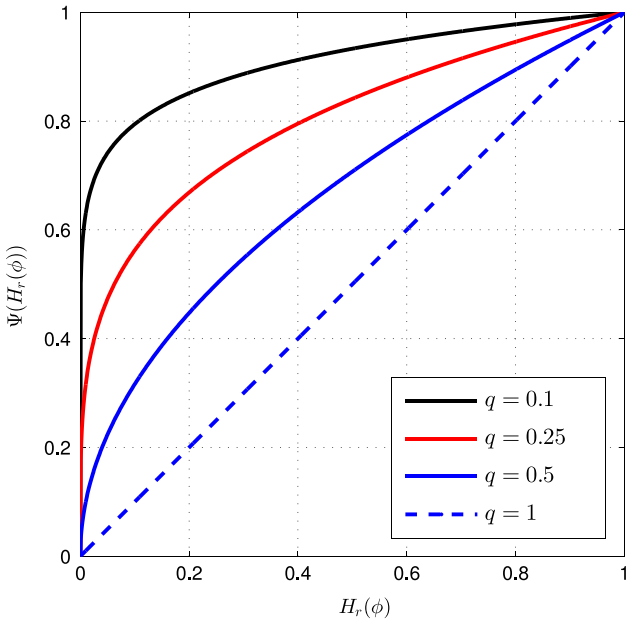

Fig. 2. Function $\Psi(H_r(\phi))$ for different values of q.

2.4. Stress constraint definition

Based on the same arguments of [35], the continuum constraint $g(\sigma(\mathbf{u}))$ in (8) is substituted by a finite number of stress constraints g_r defined at sample points $\mathbf{x}_r \in D, r = 1, \ldots, N_r$. The number and distribution of these sample points must be a consistent approximation of the continuum case. Moreover, only points $\mathbf{x}_r$ belonging to Ω must be effectively considered within the constraint set. A stress constraint g_r that takes continuous values as long as the boundary $\partial\Omega$ passes over a sample point during its movement is given by:

$$g_r(\mathbf{u}, \phi) = \Psi(H_r(\phi)) \frac{\sigma_r^{vM}}{\sigma_{adm}} - 1 \leq 0, \tag{15}$$

where

$$\Psi(H_r(\phi)) = H_r(\phi)^q, \quad H_r(\phi) = \frac{1}{a_r} \int_D I_r(\mathbf{x}) H(\phi) dD, \tag{16}$$

$$I_r(\mathbf{x}) = \begin{cases} 1, & \text{if } \mathbf{x} \in \Omega_r, \\ 0, & \text{if } \mathbf{x} \notin \Omega_r, \end{cases} \quad \text{and} \quad a_r = \int_D I_r(\mathbf{x}) dD, \tag{17}$$

$$\sigma_r^{vM} = \sqrt{\frac{3}{2} \mathbf{s}_r \cdot \mathbf{s}_r}, \quad \mathbf{s}_r = \text{dev}(\boldsymbol{\sigma}_r), \ \boldsymbol{\sigma}_r := \mathbf{C}_1 \boldsymbol{\varepsilon}_r(\mathbf{u}). \tag{18}$$

The subdomain Ω_r is a neighborhood of $\mathbf{x}(r)$ and $\boldsymbol{\varepsilon}_r(\mathbf{u})$ the strain evaluated at $\mathbf{x}_r \in D$. The function $H_r(\phi)$ computes the volumetric (area) fraction of material 1 contained in Ω_r. Function Ψ in (15) activates or deactivates the stress constraint depending on the position of the considered sample point. Points localized near the boundary are progressively considered as the area fraction $H_r(\phi)$ goes from 0 to 1. The exponent $q \in (0, 1]$ is used to make Ψ a continuum approximation of the discontinuous 0–1 function $\mathcal{F}(x)$:

$$\mathcal{F}(x) = \begin{cases} 0 & \text{if } x = 0 \\ 1 & \text{if } x \in (0, 1]. \end{cases}$$

Fig. 2 shows the behavior of $\Psi(H_r(\phi))$ for different values of q. If $q = 1$ a linear relation between Ψ (i.e. stress significance) and area fraction $H_r(\phi)$ is obtained. Conversely, if $q \to 0$, the stress of the point is completely considered as soon as a small area fraction of the sample point neighborhood is covered by material 1. Note that the stress at $\mathbf{x}_r$

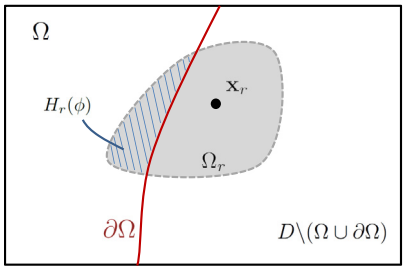

Fig. 3. Sample point $\mathbf{x}_r$ and its neighborhood Ω_r being intercepted by the border $\partial\Omega$. In this case, $\mathbf{x}_r \notin \Omega$, but the stress constraint may become active because $\Omega \cap \Omega_r \neq \emptyset$, that is, $H_r(\phi) \neq 0$.

becomes significant whenever $\Omega \cap \Omega_r \neq \emptyset$, no matter if $\mathbf{x}_r$ is strictly contained in Ω. Fig. 3 shows a sample point $\mathbf{x}_r$ whose corresponding constraint g_r might become active even though this point is outside Ω.

It is important to remark that regardless the point $\mathbf{x}_r$ is inside or outside the body, the corresponding stress $\boldsymbol{\sigma}_r$ is always calculated by Eq. (18) and the stress constraint by Eq. (15). The variable that turns this stress significant or not is the area fraction $H_r(\phi)$.

On the basis of all these considerations, the minimization problem is reformulated as follows:

Problem P_3:

$$\begin{aligned} \min_{\phi} \quad & m_\phi(\mathbf{u}) = \int_D \left[\rho(\phi) + \frac{\mu}{2}\mathbf{C}(\phi)\boldsymbol{\varepsilon}(\mathbf{u})\cdot\boldsymbol{\varepsilon}(\mathbf{u})\right] dD, \\ \text{subject to: } & \begin{cases} a_\phi(\mathbf{u},\mathbf{v}) = l_\phi(\mathbf{v}), & \forall \mathbf{v} \in V, \\ g_r(\mathbf{u},\phi) \leq 0, & r = 1,\ldots,N_r \end{cases} \end{aligned} \tag{19}$$

where $g_r(\mathbf{u},\phi)$ is given by (15) and N_r is the total number of sample points $\mathbf{x}_r$ in D.

2.5. Augmented Lagrangian-based formulation

In augmented Lagrangian approach [45,46], the constraints are included into the objective function by means of a penalization comprised by linear and quadratic terms. It is then defined a sequence $\{\alpha_r^k\}$, $k = 1, 2, \ldots$ converging to the Lagrange multipliers α_r that satisfy the necessary optimality conditions of P_3. The problem then takes the new form:

Problem P_4: for given values of penalization factor c^k and Lagrange multipliers α_r^k, solve the minimization

$$\min_{\phi} \quad J^k(\phi) = \int_D \left[\rho(\phi) + \frac{\mu}{2}\mathbf{C}(\phi)\boldsymbol{\varepsilon}(\mathbf{u})\cdot\boldsymbol{\varepsilon}(\mathbf{u})\right] dD + \sum_{r=1}^{N_r}\left\{\alpha_r^k h_r(\mathbf{u},\phi) + \frac{c^k}{2}\left[h_r(\mathbf{u},\phi)\right]^2\right\}, \tag{20}$$

$$\text{subject to: } a_\phi(\mathbf{u},\mathbf{v}) = l_\phi(\mathbf{v}), \quad \forall \mathbf{v} \in V, \tag{21}$$

where $\mathbf{u}$ is the solution of (21) and $h_r(\mathbf{u},\phi)$ is a function of the rth stress constraint given by [45,46]:

$$h_r(\mathbf{u},\phi) = \max\left\{g_r(\mathbf{u},\phi); -\frac{\alpha_r^k}{c^k}\right\}. \tag{22}$$

Once the minimum is achieved (or after a conveniently specified number of iterations), verify the condition:

$$\left|\alpha_r^k g_r^k\right| < \varepsilon, \tag{23}$$

where ε is a small tolerance. If (23) is not satisfied, update the Lagrange multipliers and penalization factor:

$$\begin{aligned} \alpha_r^{k+1} &= \max\left\{\alpha_r^k + c^k g_r^k; 0\right\}, \\ c^{k+1} &= \beta c^k, \quad \beta > 1,\ 0 < c^k < c_{\max},\ \forall k \in N. \end{aligned} \tag{24}$$

Let $k = k + 1$ and restart the process.

3. Optimization by moving the level set

Many works in the literature employ the conventional level set method to the front propagation. This method consists of modifying ϕ by taking advantage of the level set equation [36,42,47]

$$\frac{\partial \phi(\mathbf{x}(t),t)}{\partial t} - v_n(\mathbf{x}(t))\|\nabla\phi(\mathbf{x}(t),t)\| = 0, \tag{25}$$

where v_n is the velocity normal to the boundary $\partial\Omega$, that is, for all $\mathbf{x}(t)$ with $\phi(\mathbf{x}(t)) = 0$. The conventional numerical solution of (25) has a well known drawback for the present application which is the need of reinitialization of ϕ after a certain number of time steps [22,23]. This reshaping of ϕ (generally as a signed distance function) is particularly harmful at the end of the minimization process since the undesired boundary movements caused by reinitialization hinder complete convergence.

Another drawback attributed to level set minimization approaches guided by Hamilton–Jacobi evolutions is that it precludes the creation of new holes, which is an important feature in a true topological optimization method.

In order to overcome the difficulties mentioned above, the level set evolution technique proposed in Yamada et al. [40] will be used in the present work. To this aim, the topology optimization problem is modified by adding a regularization term[1]:

$$\min_{\phi} \quad J_R(\phi) = J(\phi) + \int_D \frac{1}{2}\tau\,|\nabla\phi|^2\,dD, \tag{26}$$

where $J_R(\phi)$ is the regularized objective functional and $\tau > 0$ is a diffusion coefficient that controls the effect of the regularization. Actually, this term works like a perimeter regularization that is commonly used to guarantee existence of solutions and to impose geometric constraints. Yamada et al. [40] relates the derivative of the cost function (26) to the time evolution of the level set function ϕ as follows:

$$\frac{\partial\phi}{\partial t} = -\frac{dJ_R(\phi)}{d\phi}, \tag{27}$$

where t is a pseudo-time variable. In this way, the evolution of ϕ will stop when the first order optimality condition of the minimization problem (26) is satisfied. The gradient of $J_R(\phi)$ is given by

$$\frac{dJ_R(\phi)}{d\phi} = \frac{dJ(\phi)}{d\phi} - \tau\Delta\phi, \tag{28}$$

where Δ denotes the Laplacian operator. Details to obtain the above expression are presented in the Appendix.

Substituting (28) into (27), the resulting time evolution equation with boundary and initial conditions is summarized as follows:

$$\begin{cases} \dfrac{\partial\phi}{\partial t} = \tau\Delta\phi - \dfrac{dJ(\phi)}{d\phi}, & \text{in } D \\ \phi(t=0) = \phi_0 & \text{in } D \cup \partial D \\ \dfrac{\partial\phi}{\partial \mathbf{n}} = 0, & \text{on } \partial D \backslash \partial D_N \\ \phi = 1, & \text{on } \partial D_N. \end{cases} \tag{29}$$

The first line of (29) is a reaction–diffusion equation, also known as Allen–Cahn equation. The term $\tau\Delta\phi$ represents the diffusion while the derivative of the cost function $dJ(\phi)/d\phi$ is the reaction term that accounts for the change of the shape and topology. It should be noted that boundary ∂D_N is kept fixed during the evolution of ϕ.

Furthermore, the level set function is constrained to satisfy the following conditions:

$$\begin{array}{ll} -1 \le \phi(\mathbf{x}) < 0, & \forall \mathbf{x} \in D\backslash(\Omega \cup \partial\Omega), \\ \phi(\mathbf{x}) = 0, & \forall \mathbf{x} \in \partial\Omega, \\ 0 < \phi(\mathbf{x}) \le 1, & \forall \mathbf{x} \in \Omega\backslash\partial\Omega\,. \end{array} \tag{30}$$

[1] In Yamada et al. [40] this term is called fictitious interface energy.

The evolution of ϕ by means of (27) is strongly related to the steepest descent method. In order to justify this statement, let us consider a perturbation of ϕ in the direction $\delta\phi$ to obtain the mapping

$$\phi_t = \phi + t\delta\phi. \tag{31}$$

Function ϕ_t defines the perturbed configuration Ω_t and $t \in \mathbb{R}^+$ represents the step size in the direction $\delta\phi$. The Taylor expansion of the regularized objective function is

$$J_R(\phi + t\delta\phi) = J_R(\phi) + t\frac{dJ_R(\phi)}{d\phi}[\delta\phi] + \vartheta(t^2),$$

and consequently, from (31) and (27), we can write that

$$\frac{\partial\phi_t}{\partial t} = \delta\phi = -\frac{dJ_R(\phi)}{d\phi}. \tag{32}$$

The derivative of $J_R(\phi)$ in the direction $\delta\phi$ provided by (32) is then

$$\begin{aligned}\frac{dJ_R(\phi)}{d\phi}[\delta\phi] &= \int_D \frac{dJ_R(\phi)}{d\phi}\delta\phi dD = \int_D \frac{dJ_R(\phi)}{d\phi}\left(-\frac{dJ_R(\phi)}{d\phi}\right)dD \\ &= -\int_D \left(\frac{dJ_R(\phi)}{d\phi}\right)^2 dD \leq 0.\end{aligned} \tag{33}$$

Thus, for a small enough $t > 0$, and being ϕ an element different from that satisfies the optimality condition, the value of J_R decreases:

$$J_R(\phi + t\delta\phi) = J_R(\phi) - t\int_D \left(\frac{dJ_R(\phi)}{d\phi}\right)^2 dD < J_R(\phi). \tag{34}$$

This concludes that (29) should drive the function ϕ for a feasible local solution of the structural topology optimization problem.

3.1. Sensitivity analysis

This section is devoted to calculate the reaction term $dJ(\phi)/d\phi$ used in the evolution equation (29). It is worth emphasizing that $J(\phi)$ includes already the penalization terms (via augmented Lagrangian) corresponding to stress constraints. However its total derivative $dJ(\phi)/d\phi = dJ(\mathbf{u}(\phi), \phi)/d\phi$ must take into account the satisfaction of the state equation (21). To this aim, the well known adjoint method was used, that may be formally derived by introducing a Lagrangian function $\pounds$ defined as the sum of function $J(\mathbf{u}, \phi)$ and the state constraint, considering the fields ϕ, $\mathbf{u}$ and $\boldsymbol{\lambda}$ as independent variables:

$$\begin{aligned}\pounds(\phi, \mathbf{u}, \boldsymbol{\lambda}) &= J(\mathbf{u}, \phi) + a_\phi(\mathbf{u}, \boldsymbol{\lambda}) - l_\phi(\boldsymbol{\lambda}) \\ &= \int_D \left[\rho(\phi) + \frac{\mu}{2}\mathbf{C}(\phi)\boldsymbol{\varepsilon}(\mathbf{u})\cdot\boldsymbol{\varepsilon}(\mathbf{u})\right]dD + \sum_{r=1}^{Nr}\left\{\alpha_r h_r(\mathbf{u}, \phi)\right. \\ &\quad \left. + \frac{c}{2}[h_r(\mathbf{u}, \phi)]^2\right\} + a_\phi(\mathbf{u}, \boldsymbol{\lambda}) - l_\phi(\boldsymbol{\lambda}).\end{aligned} \tag{35}$$

The total variation of $\pounds$ with respect to ϕ, $\mathbf{u}$ and $\boldsymbol{\lambda}$ is then

$$\delta\pounds(\phi, \mathbf{u}, \boldsymbol{\lambda}) = \frac{\partial\pounds}{\partial\phi}[\delta\phi] + \frac{\partial\pounds}{\partial\mathbf{u}}[\delta\mathbf{u}] + \frac{\partial\pounds}{\partial\boldsymbol{\lambda}}[\delta\boldsymbol{\lambda}], \tag{36}$$

where $\delta\phi$, $\delta\mathbf{u}$ and $\delta\boldsymbol{\lambda}$ are admissible variations of the respective arguments. Consider now the set $(\phi, \mathbf{u}, \boldsymbol{\lambda})$ such that the following conditions are satisfied:

$$\frac{\partial\pounds}{\partial\boldsymbol{\lambda}}(\phi, \mathbf{u}, \boldsymbol{\lambda})[\delta\boldsymbol{\lambda}] = 0 \quad \forall\delta\boldsymbol{\lambda} \in V \quad \text{and} \quad \frac{\partial\pounds}{\partial\mathbf{u}}(\phi, \mathbf{u}, \boldsymbol{\lambda})[\delta\mathbf{u}] = 0 \quad \forall\delta\mathbf{u} \in V. \tag{37}$$

The solution of $(37)_1$ retrieves the state equation (21):

$$\frac{\partial \pounds}{\partial \boldsymbol{\lambda}}[\delta\boldsymbol{\lambda}] = a_\phi(\mathbf{u}, \delta\boldsymbol{\lambda}) - l_\phi(\delta\boldsymbol{\lambda}) = 0 \quad \forall \delta\boldsymbol{\lambda} \in V. \tag{38}$$

The second condition $(37)_2$ gives what is commonly known as adjoint equation, whose solution provides the adjoint field $\boldsymbol{\lambda}$:

$$\frac{\partial \pounds}{\partial \mathbf{u}}[\delta\mathbf{u}] = \frac{\partial J(\mathbf{u},\phi)}{\partial \mathbf{u}}[\delta\mathbf{u}] + a_\phi(\delta\mathbf{u}, \boldsymbol{\lambda}) = 0 \quad \forall \delta\mathbf{u} \in V \tag{39}$$

or, equivalently,

$$\int_D \mathbf{C}(\phi)\,[\mu\boldsymbol{\varepsilon}(\mathbf{u}) + \boldsymbol{\varepsilon}(\boldsymbol{\lambda})] \cdot \boldsymbol{\varepsilon}(\delta\mathbf{u}) dD = -\sum_{r=1}^{Nr} [\alpha_r + c h_r(\mathbf{u}, \phi)]\, \mathbf{C}_r \mathbf{A}_r(\mathbf{u}, \phi) \cdot \boldsymbol{\varepsilon}_r(\delta\mathbf{u}) \quad \forall \delta\mathbf{u} \in V. \tag{40}$$

Here $\mathbf{A}_r(\mathbf{u}, \phi)$ is a tensor that contains the derivatives of the stress constraints with respect to the stress invariants I_1, J_2 and J_3, given by

$$\mathbf{A}_r(\mathbf{u}, \phi) = \frac{\partial h_r(\mathbf{u}, \phi)}{\partial I_1}\mathbf{I} + \frac{\partial h_r(\mathbf{u}, \phi)}{\partial J_2}\mathbf{P}^T\mathbf{s}_r(\mathbf{u}) + \frac{\partial h_r(\mathbf{u}, \phi)}{\partial J_3}\mathbf{P}^T\mathbf{s}_r(\mathbf{u})\mathbf{s}_r(\mathbf{u}), \tag{41}$$

where

$$\mathbf{s}_r(\mathbf{u}) = \mathbf{P}\boldsymbol{\sigma}_r(\mathbf{u}), \quad \mathbf{P} = \mathbf{II} - \frac{1}{3}\mathbf{I}\otimes\mathbf{I}, \tag{42}$$

is the tensor of deviatoric stresses. More information about the calculation of tensor $\mathbf{A}_r(\mathbf{u}, \phi)$ is provided in [35]. Finally, the partial derivative of $\pounds(\phi, \mathbf{u}, \boldsymbol{\lambda})$ with respect to ϕ is

$$\begin{aligned}\frac{\partial \pounds}{\partial \phi}[\delta\phi] = &\int_D \left\{(\rho_1 - \rho_2) + p(\mathbf{C}_1 - \mathbf{C}_2)H(\phi)^{p-1}\left[\frac{\mu}{2}\boldsymbol{\varepsilon}(\mathbf{u}) + \boldsymbol{\varepsilon}(\boldsymbol{\lambda})\right] \cdot \boldsymbol{\varepsilon}(\mathbf{u})\right\} \frac{\partial H(\phi)}{\partial \phi}[\delta\phi]\, dD \\ &+ \sum_{r=1}^{Nr}\left\{[\alpha_r + c h_r(\mathbf{u}, \phi)]\frac{\partial h_r(\mathbf{u}, \phi)}{\partial \phi}[\delta\phi]\right\} \quad \forall \mathbf{u}, \boldsymbol{\lambda} \in V.\end{aligned} \tag{43}$$

Since $h_r(\mathbf{u}, \phi) = \max\left\{g_r(\mathbf{u}, \phi); -\frac{\alpha_r}{c}\right\}$, two possible expressions are achievable for its derivative:

1. If $h_r(\mathbf{u}, \phi) = g_r(\mathbf{u}, \phi)$, then

$$\frac{\partial h_r(\mathbf{u}, \phi)}{\partial \phi}[\delta\phi] = \frac{\sigma_r^{vM}}{\sigma_{adm}}\frac{\partial \Psi(H_r(\phi))}{\partial H_r(\phi)}\frac{\partial H_r(\phi)}{\partial \phi}[\delta\phi], \tag{44}$$

$$\frac{\partial H_r(\phi)}{\partial \phi}[\delta\phi] = \frac{1}{a_r}\int_D I_r(\mathbf{x})\frac{\partial H(\phi)}{\partial \phi}[\delta\phi]\, dD, \tag{45}$$

and thus,

$$\frac{\partial h_r(\mathbf{u}, \phi)}{\partial \phi}[\delta\phi] = \int_D \frac{I_r(\mathbf{x})}{a_r}\frac{\sigma_r^{vM}}{\sigma_{adm}}\frac{\partial \Psi(H_r(\phi))}{\partial H_r(\phi)}\frac{\partial H(\phi)}{\partial \phi}[\delta\phi]\, dD. \tag{46}$$

2. If $h_r(\mathbf{u}, \phi) = -\frac{\alpha_r}{c}$, then

$$\frac{\partial h_r(\mathbf{u}, \phi)}{\partial \phi}[\delta\phi] = 0. \tag{47}$$

Let us call upon the identity[2]

$$\frac{\partial H(\phi)}{\partial \phi}[\delta\phi] = \delta(\phi)\delta\phi,$$

where $\delta(\phi)$ is the Dirac function.

To end this issue, let us assume that the set $(\phi, \mathbf{u}, \boldsymbol{\lambda})$ satisfies the state and adjoint equations (37). In this case, the total variation of the Lagrangian function $\delta\pounds$ reduces to its partial derivative with respect to ϕ (see Eq. (36)). Moreover, it is easy to see by simple substitution, that this partial derivative corresponds to the required total derivative $dJ(\phi)/d\phi$ (see e.g. [22]):

$$\delta\pounds(\phi, \mathbf{u}, \boldsymbol{\lambda}) = \frac{\partial \pounds}{\partial \phi}[\delta\phi] = \frac{dJ(\phi)}{d\phi}[\delta\phi] = \left(\frac{dJ(\phi)}{d\phi}, \delta\phi\right) = \int_D V(\phi)\delta(\phi)\delta\phi dD. \tag{48}$$

Since $\delta\phi$ is any test function, it is possible to state formally that the derivative of the objective function is given by the field

$$\frac{dJ(\phi)}{d\phi} = V(\phi)\delta(\phi), \tag{49}$$

where

$$V(\phi) = \begin{cases} (\rho_1 - \rho_2) + p(\mathbf{C}_1 - \mathbf{C}_2)H(\phi)^{p-1}\left(\dfrac{\mu}{2}\boldsymbol{\varepsilon}(\mathbf{u}) + \boldsymbol{\varepsilon}(\boldsymbol{\lambda})\right)\cdot\boldsymbol{\varepsilon}(\mathbf{u}) \\ \quad + \displaystyle\sum_{r=1}^{Nr}\left\{[\alpha_r + c g_r(\mathbf{u},\phi)]\,\frac{I_r(\mathbf{x})}{a_r}\,\frac{\sigma_r^{vM}}{\sigma_{adm}}\,\frac{\partial \Psi(H_r(\phi))}{\partial H_r(\phi)}\right\}, \quad \text{if } g_r(\mathbf{u},\phi) \geq -\dfrac{\alpha_r}{c}, \\ (\rho_1 - \rho_2) + p(\mathbf{C}_1 - \mathbf{C}_2)H(\phi)^{p-1}\left(\dfrac{\mu}{2}\boldsymbol{\varepsilon}(\mathbf{u}) + \boldsymbol{\varepsilon}(\boldsymbol{\lambda})\right)\cdot\boldsymbol{\varepsilon}(\mathbf{u}), \quad \text{if } g_r(\mathbf{u},\phi) < -\dfrac{\alpha_r}{c}, \end{cases} \tag{50}$$

is a (velocity of evolution) field defined over D. Two important terms distinguish $V(\phi)$ given by (50) from its analogous expression in [35]. The first one is the compliance term due to coefficient μ. The other is the Heaviside function that is always present in the second term of the right side of (50) due to the exponent $p > 1$ in expression (12). Thus, the Heaviside function controls the inclusion/exclusion of this term, depending on whether the point is inside or outside the material region. As a consequence, the "islands" of material (or as written in [28], the pathological structures with small stiffness) from the design space that arise during the optimization process are eliminated.

3.2. Treatment and regularization on the reaction term (velocity field)

As shown in (34), the regularized objective function decreases if perturbed in a direction opposite to its gradient, given by Eq. (28), also the right-hand side of the reaction–diffusion problem (29). In other words, the numerical time integration of (29) provides finite updates of ϕ that decrease the objective function for small enough time steps. It is worth emphasizing that it is the reaction term of the gradient (28) who in fact contains the information for feasible topology changes, defining the velocity $V(\phi)$ in (49) and (50).

Borrowing analogous ideas found in mathematical programming, the updating direction $V(\phi)$, while keeping its descent properties, can be modified to improve the minimization sequence.

The first proposed modification is to extend the reaction term $dJ(\phi)/d\phi$ to the whole domain, eliminating the Dirac function in (49) and assuming the equality

$$\frac{dJ}{d\phi} = V(\phi). \tag{51}$$

In this way the reaction term is allowed to take any value (including zero) on D and consequently to generate changes in the level set function that lead to nucleation of new holes in the interior of the domain.

[2] Verify the distinction in notation between the variation $\delta\phi$ and the Dirac function $\delta(\phi)$.

The second proposed improvement was already pointed out in [35] and it is related to the severe variations in the amplitude of $V(\phi)$ as a consequence of local stress constraints naturally appearing because of arbitrary moving geometries. This characteristic has the undesirable effect of locking the boundary: only very limited portions of the boundary move, while all the rest remains unchanged. To avoid this effect, we employ the following scaling of $V(\phi)$:

$$V_{\log}(\phi) = \begin{cases} \ln(V(\phi)+1), & \text{if } V(\phi) \geq 0, \\ -\ln(-V(\phi)+1), & \text{if } V(\phi) < 0. \end{cases} \tag{52}$$

The last improvement of the field $V(\phi)$ refers to smoothing operators. Here we use the smoothing scheme proposed in [48]. A new velocity $\bar{V}(\phi) \in H^1(D)$ more regular than $V_{\log}(\phi)$ is obtained by solving the variational problem

$$\int_D \left(\kappa \nabla \bar{V}(\phi) \cdot \nabla X + \bar{V}(\phi) X\right) dD = \int_D X V_{\log}(\phi) dD, \quad \forall X \in H^1(D) \tag{53}$$

where $\kappa > 0$ is a small smoothing-regularization parameter. Thus, $\bar{V}(\phi)$ intrinsically takes more regularity due to the classical regularity theory for elliptic equations.

Finally, the velocity $\bar{V}(\phi)$ is normalized by

$$v(\phi) = C \frac{\bar{V}(\phi)}{\max(|\bar{V}(\phi)|)}, \tag{54}$$

where C is a weight factor. Therefore, the reaction–diffusion equation solved is:

$$\begin{cases} \dfrac{\partial \phi}{\partial t} = \tau \Delta \phi - v(\phi) & \text{in } D \\ \phi(t=0) = \phi_0 & \text{in } D \cup \partial D \\ \nabla \phi \cdot \mathbf{n} = \dfrac{\partial \phi}{\partial \mathbf{n}} = 0 & \text{on } \partial D \backslash \partial D_N \\ \phi = 1 & \text{on } \partial D_N \end{cases} \tag{55}$$

where $v(\phi)$ is given by (54).

4. Discretization and numerical implementation

In this section, the optimization algorithm is presented and some implementation aspects are discussed. The state equation (8) and the adjoint equation (40) are solved by the finite element method (FEM). Although the proposed framework for introducing local stress constraints could be used in 2D and 3D problems, only 2D numerical examples under plane stress state were tested at the present stage. A single mesh is used to discretize the level set function and to the analysis of finite elements, which uses a quadrilateral bilinear element.

The approximation of the material area fraction within each element was computed using the code available in [43], where an exact Heaviside function is used to relate the level set function to element densities.

To solve the system of time evolutionary equation (55), we employ a scheme similar to [40] and [41]. For the time discretization the implicit scheme is used and the domain D is discretized based on FEM. Thus the discretized evolution equation is given by:

$$\begin{cases} \left(\dfrac{1}{\Delta t}\mathbf{T}_1 + \tau \mathbf{T}_2\right) \boldsymbol{\Phi}_{t+1} = \mathbf{T}_1 \left(\dfrac{1}{\Delta t}\boldsymbol{\Phi}_t - \mathbf{v}\right), & \text{in } D \\ \phi(t) = 1, & \text{on } \partial D_N, \end{cases} \tag{56}$$

where

$$\mathbf{T}_1 = \bigcup_e \int_{D_e} \overset{e}{\mathbf{N}}{}^T \overset{e}{\mathbf{N}} dD, \tag{57}$$

$$\mathbf{T}_2 = \bigcup_e \int_{D_e} \nabla \overset{e}{\mathbf{N}}{}^T \nabla \overset{e}{\mathbf{N}} dD. \tag{58}$$

Here, Δt is the time increment, e is the number of elements, $\bigcup_e$ represents the union set of elements, $\mathbf{N}$ is the interpolation function and $\mathbf{v}$ is the velocity array (discrete version of $v(\phi)$). Therefore, the updated level set field $\boldsymbol{\Phi}_{t+1}$ can be obtained by solving Eq. (56).

Similarly, problem (53) was also solved using FEM and the array $\bar{\mathbf{V}}$ (discrete version of $\bar{V}(\phi)$) is obtained from the linear equation system

$$(\mathbf{T}_1 + \kappa \mathbf{T}_2)\, \bar{\mathbf{V}} = \mathbf{T}_1\, \mathbf{V}_{\log}. \tag{59}$$

In numerical practice a value of κ between 1 and 2 times $(\Delta x)^2$ is used, with Δx being the minimum grid size. High values of κ may smooth too much the reaction term field (this means that the function might miss important relevant information somewhere) leading the algorithm to an undesirable local minimum.

As already pointed out, the evolution of the level set function based on the numerical solution of the Hamilton–Jacobi equation has the known drawback of degrading the smoothness of $\boldsymbol{\Phi}$ and forcing its reinitialization using a signed distance function. Note that the explicit first order upwind scheme to solve the Hamilton–Jacobi equation uses the numerical approximation of $\nabla \boldsymbol{\Phi}$ demanding good quality of this function near the boundaries. The present approach, on the other hand, has two advantages on this issue. Firstly, it incorporates a useful diffusion (regularization) operator $\tau \mathbf{T}_2$ in and secondly, no approximate derivatives of $\boldsymbol{\Phi}$ are needed within the algorithm. Despite these observations, a sensitivity analysis on the value of the updating $\boldsymbol{\Phi}_{t+1}$ to the different possible treatments of the array $\mathbf{v}$ (Section 3.2) is still lacking.

4.1. Optimization algorithm

It was shown in the previous sections that the minimization problem P_4 is solved by the pseudo-time evolution problem (55) and corresponding discrete version (56). The algorithm is then summarized in the succeeding text:

External loop:

1. Initialize the level set function ϕ^0 ($\Omega_0 \subset D$).
2. Define $k = 1$, $c^k > 0$, $\alpha_r^k \in \mathbb{R}$.
3. Perform the *internal loop* to minimize function $J^k(\phi, \alpha_r^k, c^k)$ obtaining ϕ^k.
4. Update c^k and α_r^k using (24).
5. $k = k + 1$. Return to step 3.

The step 3 of the *external loop*, called *internal loop,* consists of the minimization of objective function J^k for fixed given values of c^k and α_r^k. However, as indicated in [46], the minimization in 3 may be performed partially or, equivalently, substituted by a sufficient descent condition. For practical purposes this means that a fixed number of minimization iterations, say $Niter$, must be accomplished prior to the Lagrange multipliers updating in 4. Then, the iterative procedure for a sufficient decrease of $J^k(\phi, \alpha_r^k, c^k)$ is the following:

Internal loop: for $j = 1$ *to* $j \leq Niter$:

1. Obtain the discretized fields $\mathbf{u}_j$ and $\boldsymbol{\lambda}_j$ by solving, respectively, the state equation (21) and adjoint equation (40).
2. Compute the field $v_j(\mathbf{u}_j, \boldsymbol{\lambda}_j)$ based on Eq. (54).
3. Update ϕ using (56) choosing Δt_j such that $J(\phi_{j+1}) \leq J(\phi_j)$.
4. If $\left| J(\phi_{j+1}) - J(\phi_j) \right| \leq \varepsilon$, then stop the iterative process; otherwise continue.
5. $j = j + 1$. Go to step 1.

4.2. Sample points stress evaluation

In the present implementation the same choices of [35] were made for the stress sample points $\mathbf{x}_r$, making them coincide with the nodes of the finite element mesh. This distribution of sample points is consistent with the objective of enforcing the stress constraint all over the domain, following the resolution of the stress field provided by the finite element mesh. The corresponding neighborhood Ω_r is square with a length of a finite element size (Fig. 4) providing a complete covering of D.

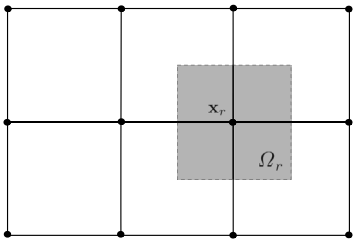

Fig. 4. Example of a sample point $\mathbf{x}_r$ (coinciding with a node of the finite element mesh) and its neighborhood Ω_r.

The discontinuous strain field provided by bilinear quadrilateral elements is recovered at a sample point $\mathbf{x}_r$ by the classical average scheme

$$\boldsymbol{\varepsilon}_r(\mathbf{x}_r) = \sum_{e=1}^{N_e} \frac{\mathbf{B}_e(\mathbf{x}_r)\mathbf{U}_e}{N_e}, \tag{60}$$

where N_e is the number of elements e attached to node $\mathbf{x}_r$, $\mathbf{B}_e(\mathbf{x}_r)$ is the array of shape function derivatives of element e, and $\mathbf{U}_e$ is the array of nodal displacements of element e. The stress at this node is then computed by (18) and the stress constraint by (15).

5. Numerical results

Several numerical tests were performed to explore the features of the proposed optimization scheme. All the examples use the following parameters: densities $\rho_1 = 1$ and $\rho_2 = 10^{-3}$, Young's modulus $E_1 = 1$ and $E_2 = 10^{-3}$ and Poisson's ratio $\nu = 0.3$. The exponent q that enhances the stress at a sample point takes the value $q = 0.5$. The Lagrange multipliers vector $\boldsymbol{\alpha}$ is initialized with a vector of zeros and updated as the rule (see expression $(24)_1$). The number of sample points N_r coincide with the number of nodes in the mesh. The mass ratio is referred as the ratio between the final mass and total mass. Moreover, the value of compliance W of the structure (given in graphs and tables) is defined as

$$W = \int_D \mathbf{C}(\phi)\boldsymbol{\varepsilon}(\mathbf{u}) \cdot \boldsymbol{\varepsilon}(\mathbf{u}) dD. \tag{61}$$

Concerning to $Niter$, we heuristically chose $Niter = 20$ fixed iterations for the internal optimization loop in most cases, unless indicated otherwise. In the convergence diagrams, each iteration corresponds to a single solution of the evolution equation (56). After some numerical tests regarding efficiency, it was chosen a convenient time step of $\Delta t \leq 0.25$. It is worth mentioning that differently from the Hamilton–Jacobi evolution procedure where due to the CFL condition many time increments Δt were needed, the present updating was performed with a single Δt time step. Numerical experiments showed that, for the tested mesh sizes, the latter approach performed faster despite the need of an additional equation-system solution at each iteration.

A relevant operational issue is related to the boundary conditions of ϕ. Since the level set function gradient has been included into the objective function and thus providing a perimeter penalization, the algorithm "prefers" designs attached to the boundaries. This observation was also reported in [4]. As a suggestion to avoid this preference, the value of ϕ of those nodes attached to the boundary $\partial D \backslash (\Gamma_D \cup \Gamma_N)$ whose associated elements have unitary density is set to $\phi = -\varepsilon$, where ε is a small value. In this work ε was set to 10^{-3}.

5.1. L-problem

This example is the classic benchmark problem of topology optimization considering stress constraints. Fig. 5 shows the model clamped at its top boundary and submitted to a force $P = 1$ N applied at the middle of the right side. The length is $L = 1$ m and the yield stress $\sigma_{adm} = 42$ Pa. Domain D was discretized with 160 elements along the longest sides in both horizontal and vertical directions giving a total of 16,384 quadrilateral finite elements and 16,705 nodes. Therefore, there exist $N_r = 16{,}705$ sample points for the stress evaluation. The optimization was run using the following parameters: $c = 0.15$ ($c_{\max} = 30c$), $\beta = 1.1$, $\mu = 0.0015$, $C = 0.25$, $p = 1.001$, $\kappa = 2(\Delta x)^2$

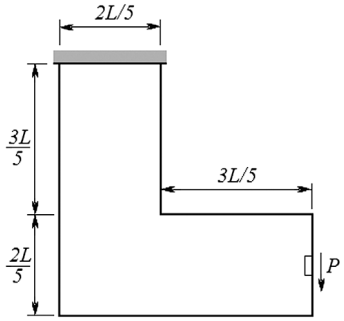

Fig. 5. L-problem: model.

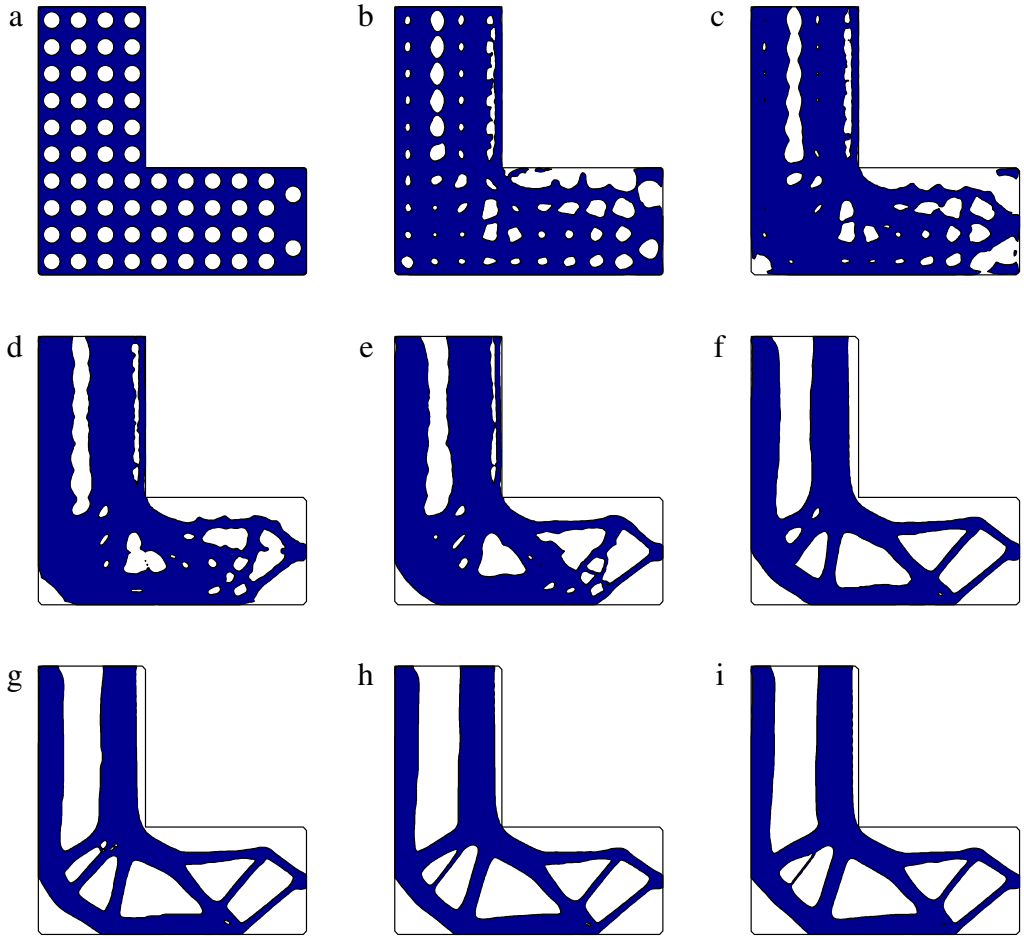

Fig. 6. L-problem: (a) initial level set domain; Intermediate results at: (b) iteration 5; (c) iteration 10; (d) iteration 20; (e) iteration 50; (f) iteration 100; (g) iteration 150; (h) iteration 600; and (i) iteration 1000.

and $\tau = 7 \times 10^{-6}$. The optimization procedure was stopped after 60 updates of external loop, though in some cases the convergence has been reached with less iterations.

Fig. 6(a) shows the initial level set domain and Fig. 6(b)–(i) show the intermediate results during the optimization process. The final design and its stress constraint distribution are presented in Fig. 7(a) and (b), respectively. Fig. 8 shows the level set function corresponding to the final design bounded between -1 and 1 according to its

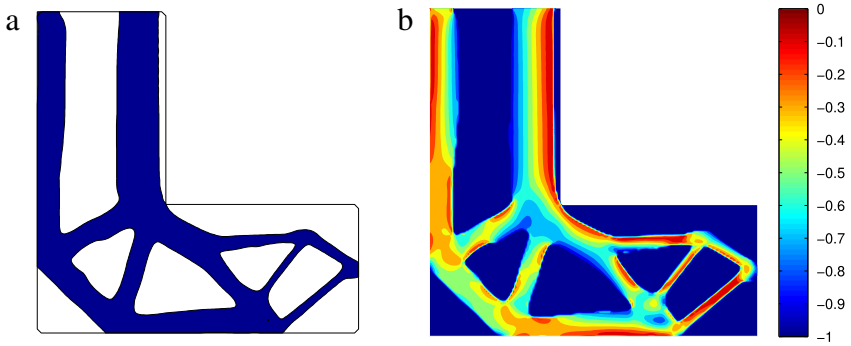

Fig. 7. L-problem: (a) final design at iteration 1200; and (b) stress constraint distribution with $\max_D(g_r) = 6.1 \times 10^{-3}$. The mass ratio is 0.4643.

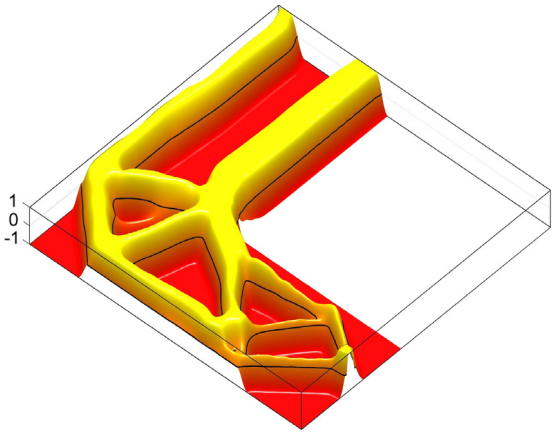

Fig. 8. L-problem: level set function of the final design.

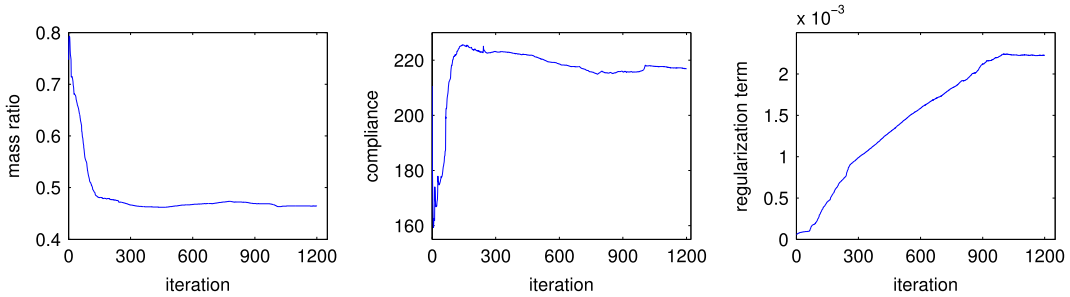

Fig. 9. L-problem: convergence history for the mass ratio, the compliance W and the regularization term.

definition (30). Fig. 9 represents the convergence history for the mass ratio, the compliance W and the regularization term. It must be noted that the compliance value shown in Fig. 9 is not multiplied by the scale factor $\mu/2$.

The same problem with the same parameters is again solved starting from the solid initial configuration (no holes) shown in Fig. 10. In the minimization sequence it is observed that the optimization algorithm identifies and eliminates firstly the stress concentration in the corner, after which it begins to nucleate holes in the design domain. The final design and its respective stress constraint function is shown in Fig. 11(a) and (b), respectively. The graphics for the convergence of the mass ratio, the compliance W and the regularization term are shown in Fig. 11(c), (d) and (e), respectively. The stable behavior of the optimization process can be verified in Fig. 12. In this figure we can observe the penalty terms (linear and quadratic) of the stress penalization terms (Eq. (20)) converging to zero as expected. Also, for the objective function is shown the convergence for each iteration and for each update of the Lagrange multipliers

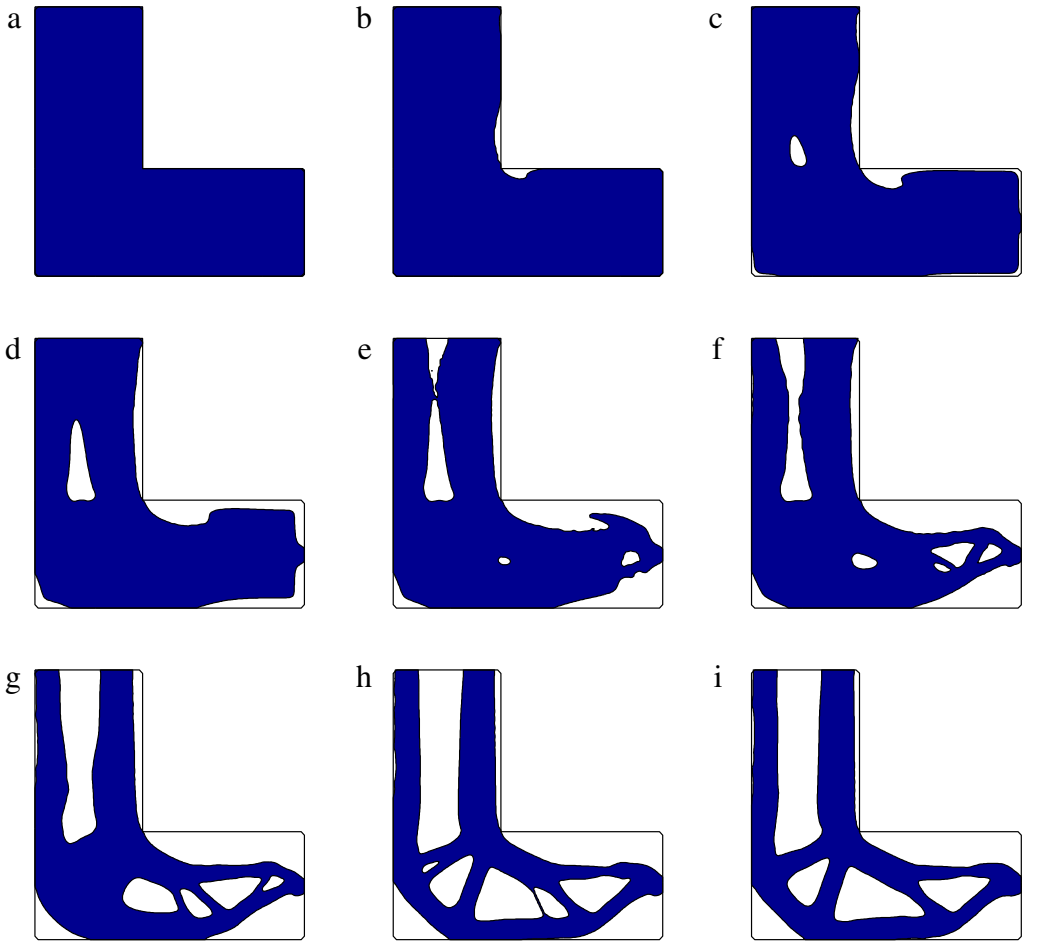

Fig. 10. L-problem: (a) initial level set domain; Intermediate results at: (b) iteration 40; (c) iteration 80; (d) iteration 110; (e) iteration 120; (f) iteration 140; (g) iteration 200; (h) iteration 600; and (i) iteration 1000.

Table 1
L-problem: Summary of results for the obtained final designs.

Final design	τ	Mass ratio	W	$\max_D(g_r)$
Fig. 7(a)	7×10^{-5}	0.4643	216.91	6.1×10^{-3}
Fig. 11(a)	7×10^{-6}	0.5066	205.78	6.8×10^{-5}
Fig. 13(b)	5×10^{-5}	0.5894	185.36	1.5×10^{-3}
Fig. 13(d)	1×10^{-5}	0.5124	210.53	3.7×10^{-3}
Fig. 13(f)	7×10^{-5}	0.5130	212.92	7.1×10^{-4}

(external loop). Note that the oscillations observed in the graph of objective function versus iterations are mostly due to the augmented Lagrangian actualization steps, where each of the stress Lagrange multipliers are updated.

Finally, we analyze the effect of the regularization parameter τ. In order to verify the capability of our optimization algorithm provide a local feasible solution for arbitrary initializations (that is, with or without holes), we changed again the initial level set function (see Fig. 13(a)). Three cases were tested where τ is set to 5×10^{-5}, 1×10^{-5} and 7×10^{-6}, respectively. The corresponding final designs and the constraint distribution for each of the three cases are shown in Fig. 13. Table 1 summarizes the indicators of the final mass ratio, the compliance W and the maximum value of the stress constraint ($\max_D(g_r)$) for each final design obtained in this example.

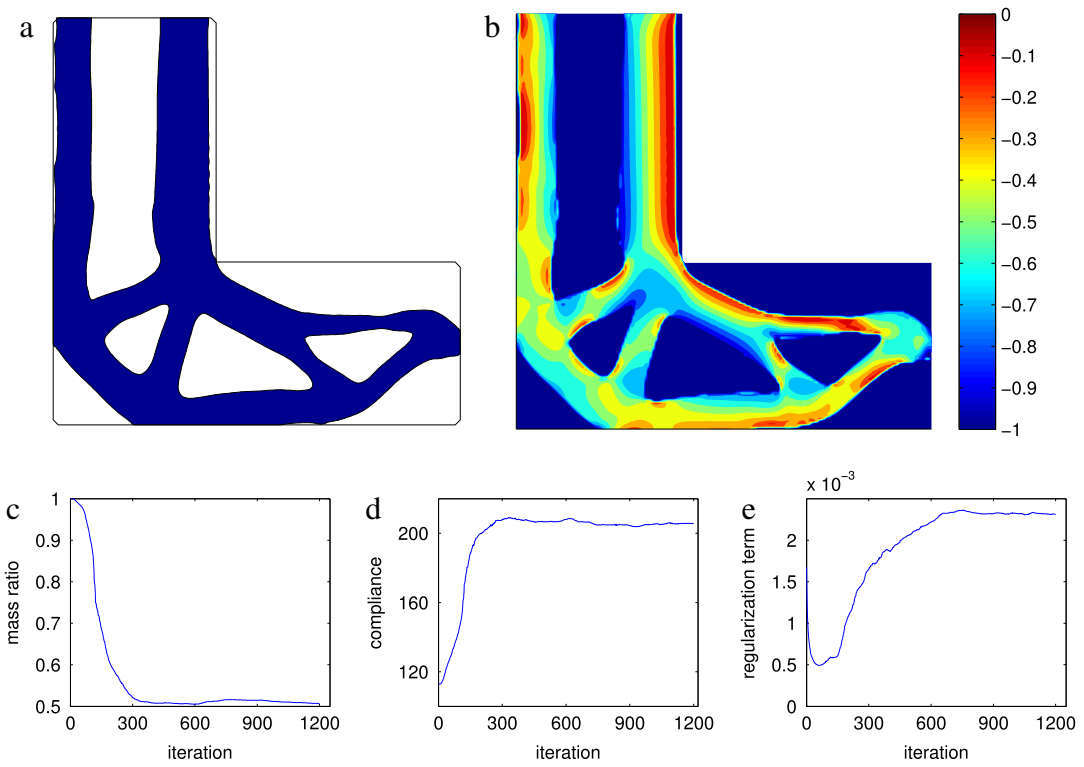

Fig. 11. L-problem: (a) final design at iteration 1200; (b) stress constraint distribution with $\max_D(g_r) = 6.8 \times 10^{-5}$; (c) convergence history for the mass ratio (final mass ratio is 0.5066); (d) compliance W convergence (final compliance value is 205.78); and (e) regularization term.

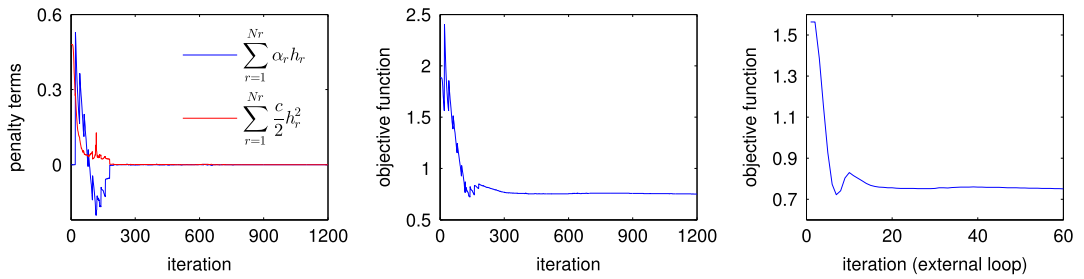

Fig. 12. L-problem: convergence history for the penalty terms and the objective function. For the objective function is shown the convergence for each iteration and for each update of the Lagrange multipliers (external loop).

It is worth noting that all optimal structures obtained at the end of the optimization process satisfy the constraints imposed on the problem in a reasonable way. Also, the final designs can be very different depending on the initial configuration. However, the stress concentration has been detected and eliminated by a rounding radius in the corner.

An analysis of the stress state of an optimal design could be useful to a deeper understanding of the problem at hand. Let us consider the case shown in Fig. 11. The first issue to be highlighted is that the optimal feasible design is quite robust with few bars, occurrence possible related to the regularization terms included within the formulation. Secondly, these few structural members are submitted not only to axial efforts but also to bending. This is clearly seen on the failure stress distribution where a stress gradient is found along the cross section of the members. This final design and stress distribution is closely comparable to that obtained in e.g. Figure 13 of [2] where a similar approach to handle local stresses but a SIMP approach was used. We noted, however, that present proposition found the optimal design with a better boundary definition. Note that in the present case the “ersatz” material is contained in a narrow band of the size of a single element.

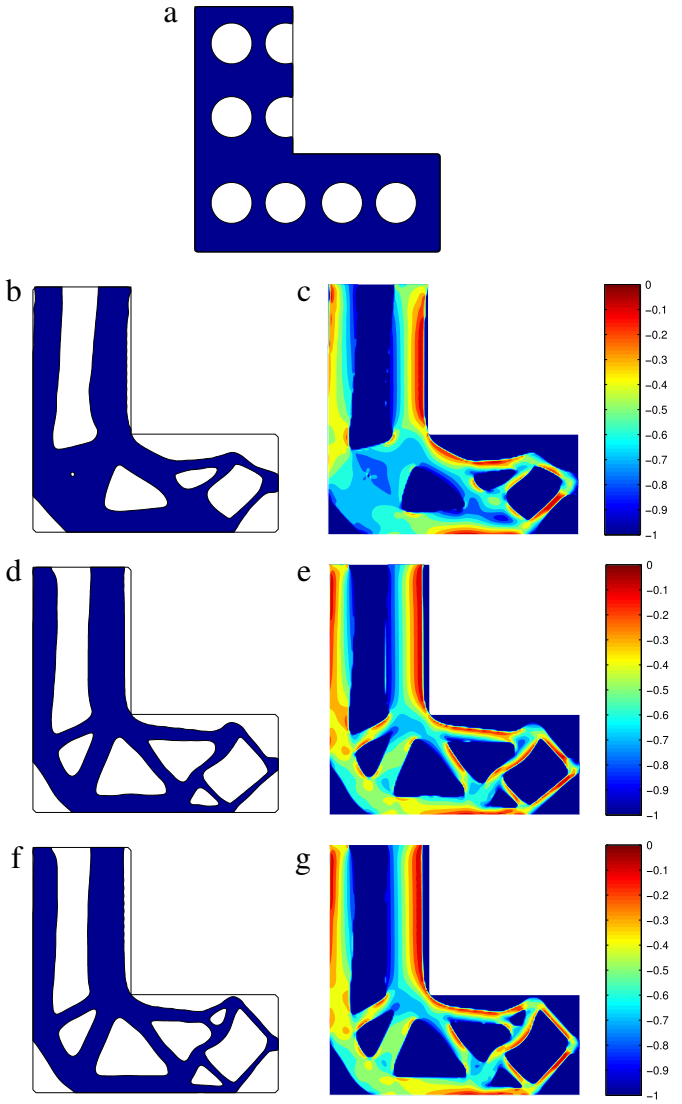

Fig. 13. L-problem: (a) initial level set domain; (b) obtained design for $\tau = 5 \times 10^{-5}$ (mass ratio = 0.5894); (c) stress constraint distribution of (b) with $\max_D(g_r) = 1.5 \times 10^{-3}$; (d) obtained design for $\tau = 1 \times 10^{-5}$ (mass ratio = 0.5124); (e) stress constraint distribution of (d) with $\max_D(g_r) = 3.7 \times 10^{-3}$; (f) obtained design for $\tau = 7 \times 10^{-6}$ (mass ratio = 0.5130); and (g) stress constraint distribution of (f) with $\max_D(g_r) = 7.07 \times 10^{-4}$.

Moreover, it is useful to note that in the way the problem is set, i.e. volume minimization subject to stress constraints, the feasible domain may be empty if the external load is sufficiently large. This would not happen if objective and constraint are switched to a stress minimization with volume constraint, as is also the case of the classical compliance problem.

5.2. Cantilever beam problem

This example deals with a cantilever beam problem. Domain D is a rectangle with a distributed vertical force $P = 1$ N applied at center of the right side and clamped at left side, as shown in Fig. 14 where $L = 1$ m. A mesh of 100×50 is used to discretize the fixed design domain, that means, $N_r = 5151$ sample points for the stress evaluation. The yield stress is $\sigma_{adm} = 19$ Pa. The optimization was run using the following parameters: $c = 0.8$ ($c_{\max} = 10c$), $\beta = 1.1$, $\mu = 0.01$, $C = 0.25$, $p = 1.1$, $\kappa = 2(\Delta x)^2$ and $\tau = 3 \times 10^{-5}$.

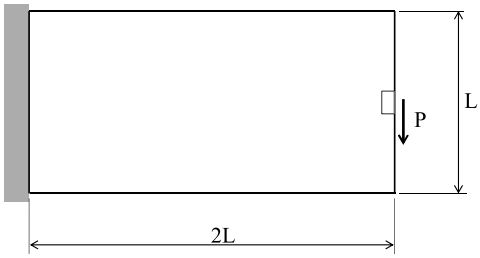

Fig. 14. Cantilever beam problem: model.

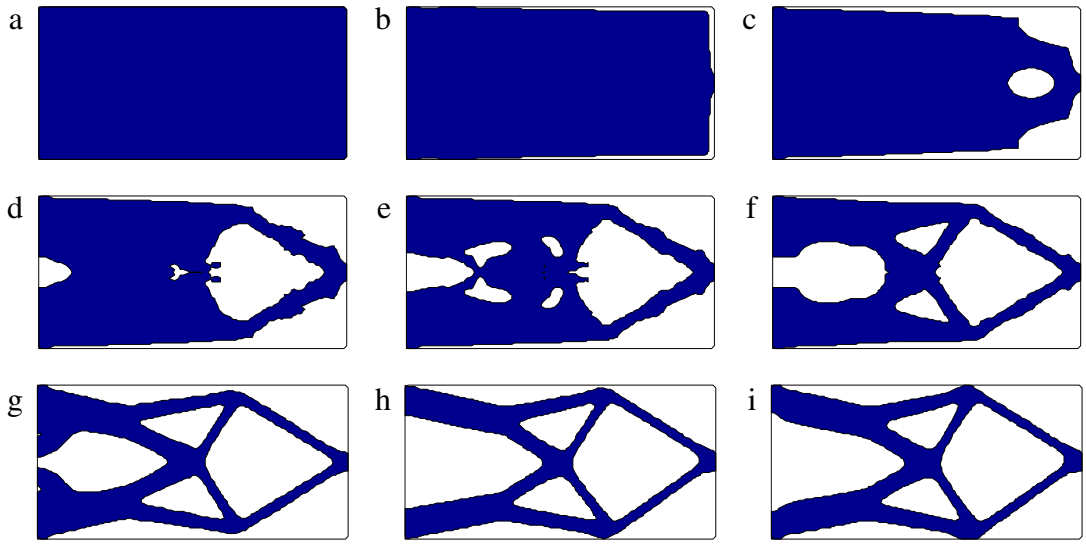

Fig. 15. Cantilever beam problem: (a) initial level set domain; Intermediate results at: (b) iteration 40; (c) iteration 45; (d) iteration 50; (e) iteration 55; (f) iteration 60; (g) iteration 150; (h) iteration 300; and (i) iteration 400.

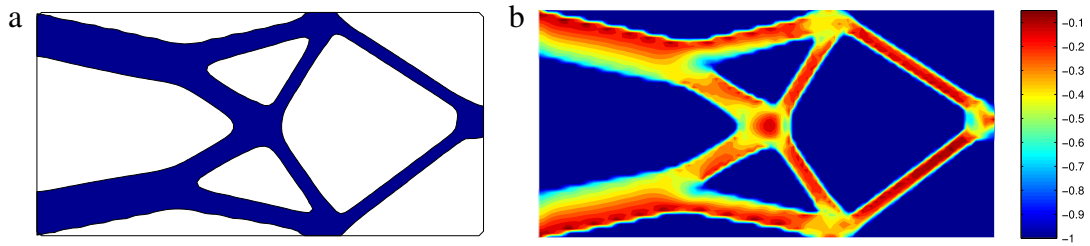

Fig. 16. Cantilever beam problem: (a) final design at iteration 600; and (b) stress constraint distribution with $\max_D(g_r) = -1.8 \times 10^{-2}$. The mass ratio is 0.3107 and the compliance value W is 118.35.

Fig. 15 presents the intermediate results during the optimization process from an initial level set domain filled with solid material. The final design is shown in Fig. 16(a) after 30 external updates (external loop). In Fig. 16(b) is shown the distribution of (nodal) stress constraints. The maximum value achieved for the constraints is $\max_D(g_r) = -1.8 \times 10^{-2}$.

We now investigate the effect that different penalization exponent p values have upon the optimal solutions for problems with stress constraint. The initial level set function is shown in Fig. 17(a). Here we used 26 updates of external loop and $Niter = 30$ for each subproblem (internal loop). The remaining parameters are the same. We examine three cases where the penalization exponent p is set to 1.001, 1.5 and 3, respectively. Fig. 17 shows the final configuration and its respective stress constraint distribution for each case. Some numerical data are reported in Table 2 for

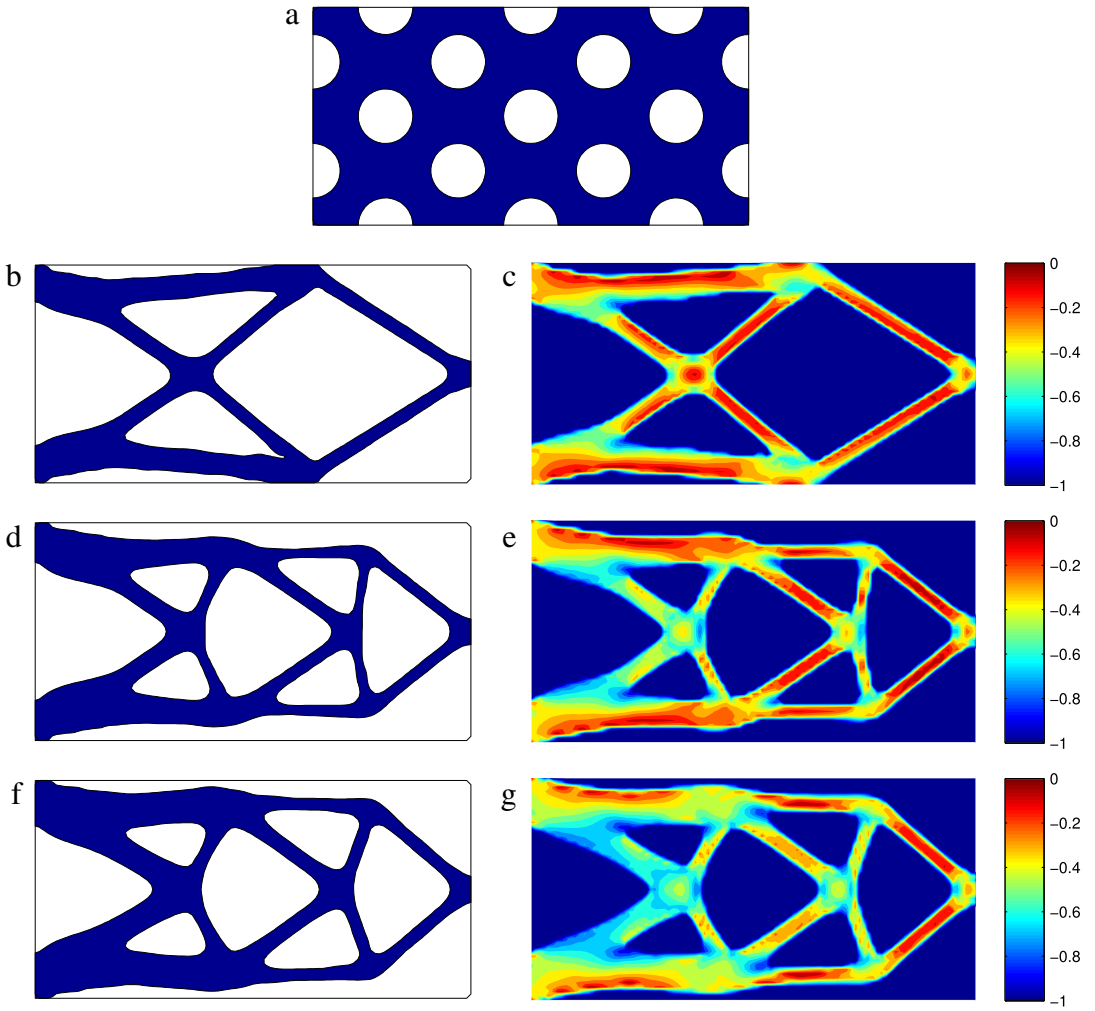

Fig. 17. Cantilever beam problem: (a) initial level set domain; (b) final design for $p = 1.001$; (c) stress constraint distribution for $p = 1.001$; (d) final design for $p = 1.5$; (e) stress constraint distribution for $p = 1.5$; (f) final design for $p = 3$; and (g) stress constraint distribution for $p = 3$.

Table 2
Cantilever beam problem: summary of the results shown in Fig. 17.

k	μ	τ	p	Mass ratio	W	$\max_D(g_r)$
$2(\Delta x)^2$	0.01	3×10^{-5}	1.001	0.2937	120.49	1.46×10^{-4}
$2(\Delta x)^2$	0.01	3×10^{-5}	1.5	0.3291	112.96	4.7×10^{-3}
$2(\Delta x)^2$	0.01	3×10^{-5}	3	0.3966	96.81	1.30×10^{-3}

comparison. Higher values of p provide lower values to the compliance of the design. On the other hand, the mass ratio also increases as p increases. This fact may be explained due to the increase of consideration of the "intermediate" elements in the structure as p increases (in the case of stress constraint problems). Fig. 18 shows the convergence history for the mass ratio and objective function, the compliance and the regularization term for the case $p = 3$.

The cantilever beam problem is often used in the literature for topology optimization problems with compliance. We used the approaches developed in the present work (regularization schemes and evolution equation) for the compliance problem. Fig. 19(a) shows the (typical) final design obtained with mass constraint set to 40% of the total mass. Fig. 19(b) shows the stress constraint distribution presenting high stress concentration at the clamp. Although the final design for compliance problem has provided a lower compliance value than for stress constraint problem

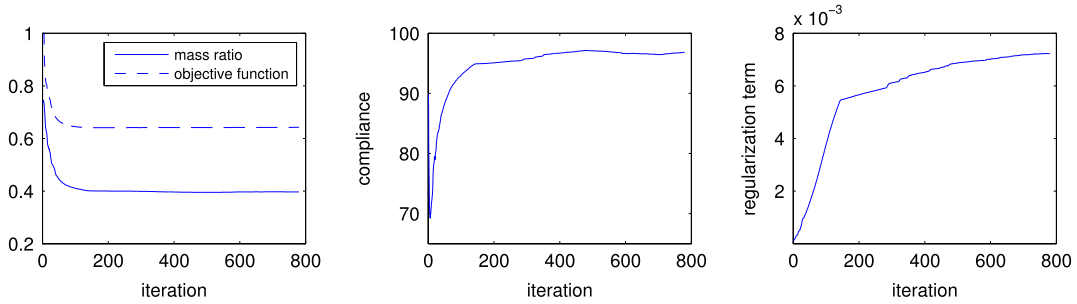

Fig. 18. Cantilever beam problem: convergence history for the mass ratio and objective function, the compliance and the regularization term for the final design shown in Fig. 17(f), where $p = 3$.

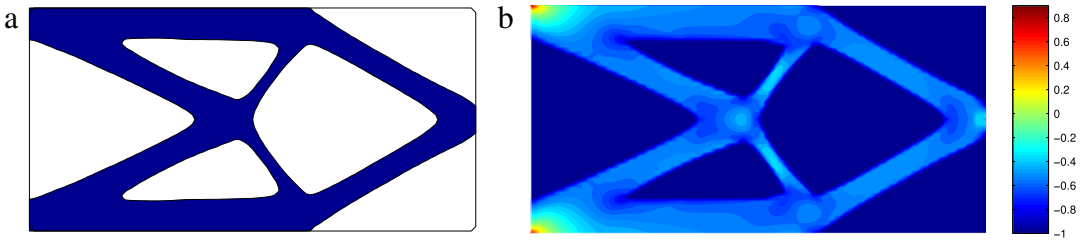

Fig. 19. Cantilever beam problem: (a) final design for the compliance problem; and (b) stress constraint distribution with $\max_D(g_r) = 0.9$. The mass constraint was set to 40% of the total mass. The compliance of the final design is 76.8. The initial configuration has the material domain filled with material.

(see Fig. 19 and Table 2 for the case $p = 3$ that have practically the same mass ratio), it has not satisfied the more common engineering requirement, that is, support loads without failure. Moreover, the final designs are significantly different (compare Figs. 17(f) and 19).

5.3. Crack problem

In this example we verify the proposed approach for a plate emulating a fracture mode I. A force $P = 1$ N is applied to open the fracture therefore producing high stresses at the fracture tip. The main objective of this example is to verify if the proposed approach is able to achieve a feasible design and a local minimum for the mass. We assume a yield stress of the material equal to $\sigma_{adm} = 23$ Pa. It will be considered two models with different geometric sizes and load locations.

The first model consists in a square plate of length $L = 1$ m and fracture length $L/2$, as shown in Fig. 20. This same example was tested in [35] and, for comparison purposes, we used the same initial level set domain (see Fig. 21(a)). Only the right symmetric part of the plate was discretized. Two mesh sizes were compared to verify the influence of the finite element mesh size on the final design. The first one was partitioned with a mesh of 100×50 elements and 5151 nodes (equal to the number of stress sample points N_r) and another one with 180×90 elements and 16,471 nodes (equal to the number of N_r). The following parameters were used to both meshes: $\beta = 1.1$, $\mu = 0.004$, $C = 0.25$ and $p = 1.001$; the remaining parameters are shown in Table 3 for each mesh. The minimization was stopped after 30 updates of external loop. Fig. 21 shows the optimal configurations with its respective stress constraint distribution for each mesh size. It is possible to observe that the dependence on the finite element mesh size is small. To achieve this feature, the penalization factor and the parameters related to the element size were appropriately changed. Comparing with [35] the designs obtained in this paper are more slender, that is, a smaller mass ratio. This occurred because of the allowance of holes nucleation within the present approach, which allows better stress distribution. The mass ratio, the compliance W and the maximum value of the stress constraint ($\max_D(g_r)$) for each mesh also are shown in Table 3.

The second model consists in a plate of length $2L \times L$ where $L = 1$ m and fracture length $L/2$, as shown in Fig. 22. Note that now the force is applied on a different location compared to model 1. Considering symmetry, a mesh of 100×100 elements is used to discretize the right half of the plate ($N_r = 10,201$). We used the following parameters: $c = 0.8$ ($c_{\max} = 20c$), $\beta = 1.1$, $\mu = 0.004$, $C = 0.25$, $p = 1.001$, $\kappa = 1(\Delta x)^2$ and $\tau = 2 \times 10^{-5}$.

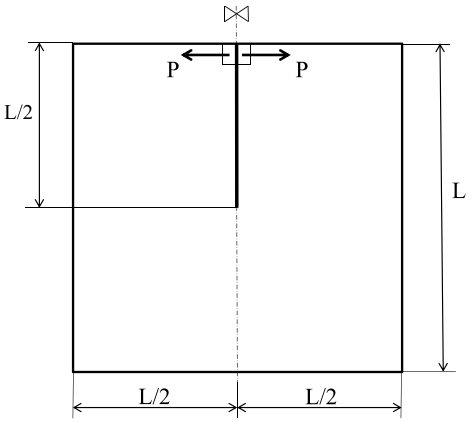

Fig. 20. Crack problem: model 1.

Table 3
Crack problem (model 1): parameters of the results shown in Fig. 21.

Mesh	k	τ	c	$c_{\max}$	Mass ratio	W	$\max_D(g_r)$
100×50	$1(\Delta x)^2$	3×10^{-5}	0.8	$10c$	0.2340	113.49	−0.0159
180×90	$2(\Delta x)^2$	1×10^{-5}	0.25	$20c$	0.2277	117.36	−0.0171

The optimization algorithm was stopped after 35 updates of external loop. In this case, the optimization process was tested for two initial configurations. Fig. 23 shows the optimal configurations as well as the distribution of the stress constraint values for each initial level set domain. Although the designs are different, the compliance and mass ratio have close values. Once again, the final design eliminates the stress singularity and a feasible design is achieved. Fig. 24 shows the 3D level set function for the optimal designs of Fig. 23(b) and (e). Fig. 25 shows the convergence history for the mass ratio and objective function, the compliance and the regularization term for the final configuration shown in Fig. 23(e).

6. Concluding remarks

The structural topology optimization problem of mass minimization under local stress constraints was addressed. An augmented Lagrangian technique associated with the stress constraint proposed in [35] was again used to transform a minimization problem with multiple constraints into a sequence of unconstrained minimization problems. The level set evolution, differently from the classical approach based on Hamilton–Jacobi equation, was controlled by a reaction–diffusion problem as proposed in [40]. Some conclusions are highlighted:

1. The optimization algorithm was clearly successful to identify high stresses and to create minimizing sequences arriving to local optimum feasible designs.
2. Numerical experiences showed that the use of the reaction–diffusion evolutionary equation (55) conferred the algorithm with good numerical behavior, allowing for quite stable optimization sequences. As already pointed out, the elimination of reinitialization operations was certainly an important feature contributing to this fact. Moreover, the algorithm uses fewer parameters than those needed for Hamilton–Jacobi based evolutions.
3. Although the velocity field V is, by means of Eq. (48), meaningful on the boundary, its extension to the complete domain D was verified to turn the algorithm capable of nucleating holes in appropriate regions, which in the present case are those with lower stresses and, consequently, the stress constraints are inactive. Thus, we did not observe significant oscillations in the objective function when a hole is inserted during the optimization process.
4. The reaction–diffusion equation used in this work was clearly inspired in that used in Yamada et al. [40] for compliance problem. Yamada et al. [40] verified that the initial level set domain has low influence on the final design. For present stress constrained problems this low-dependency was not confirmed. We hypothesize that this is due to the great number of local minima characterizing stress constrained optimization problems. Since the

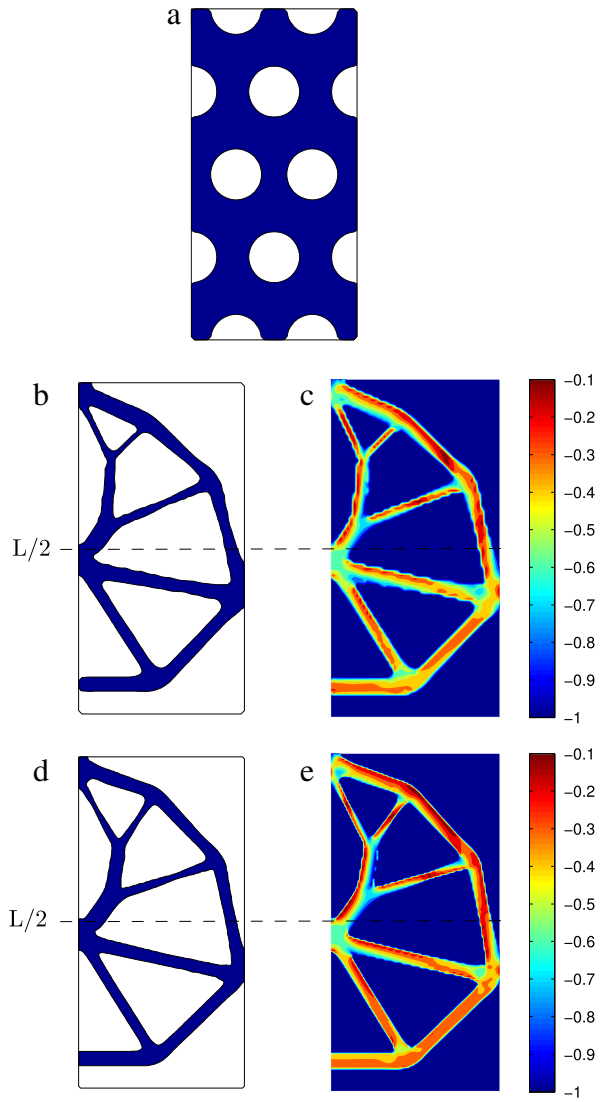

Fig. 21. Crack problem (model 1): results for different meshes; (a) initial level set domain; (b) final design for 100×50 mesh; (c) stress constraints distribution for 100×50 mesh; (d) final design for 180×90 mesh; and (e) stress constraints distribution for 180×90 mesh.

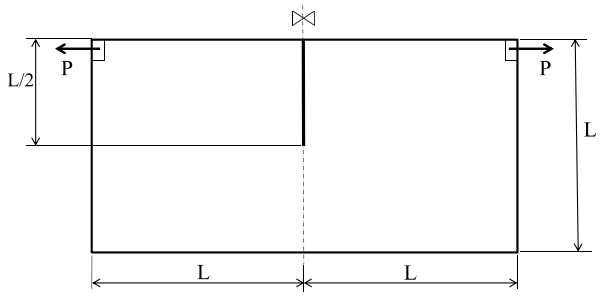

Fig. 22. Crack problem: model 2.

proposed algorithm does not guarantee to find a global optimum, the final designs still show significant dependence on the initial configuration.

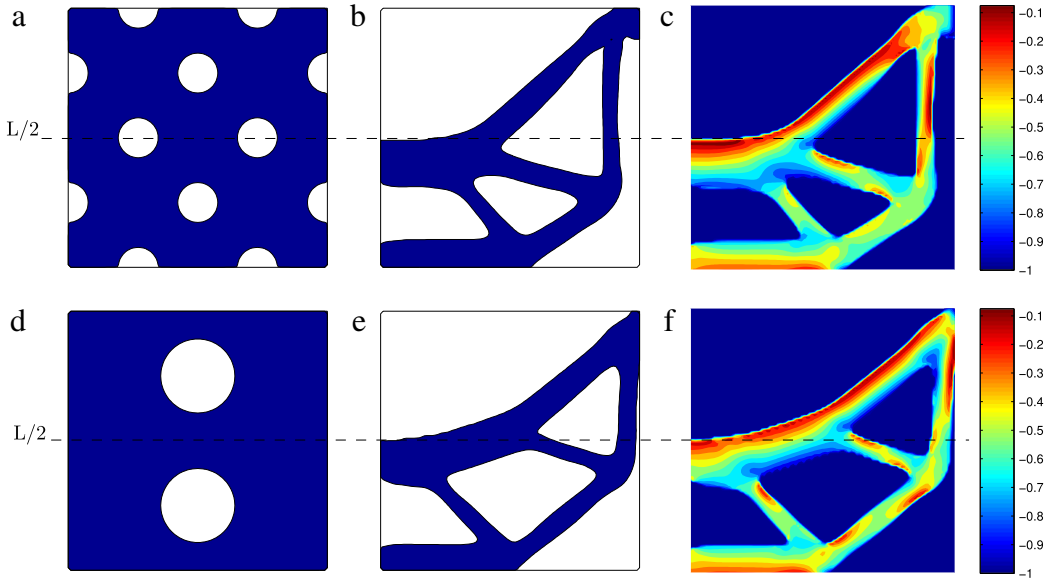

Fig. 23. Crack problem (model 2): (a) initial configuration; (b) final design (mass ratio is 0.34 and compliance W is 59.73); (c) stress constraint distribution with $\max_D(g_r) = -6.6 \times 10^{-4}$; (d) initial configuration; (e) final design (mass ratio is 0.33 and compliance W is 57.16); and (f) stress constraint distribution with $\max_D(g_r) = -3.14 \times 10^{-4}$.

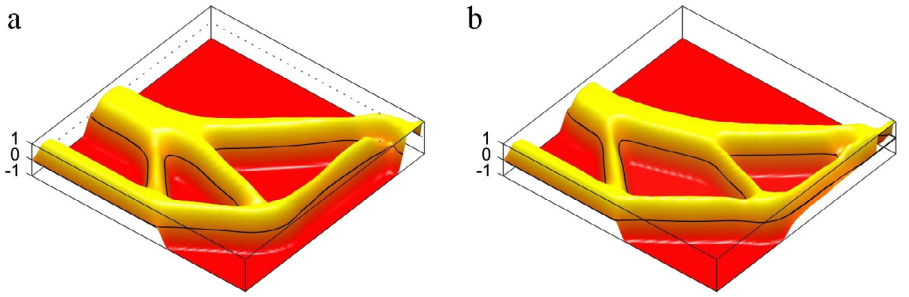

Fig. 24. Crack problem (model 2): (a) 3D level set function for Fig. 23(b); and (b) 3D level set function for Fig. 23(e).

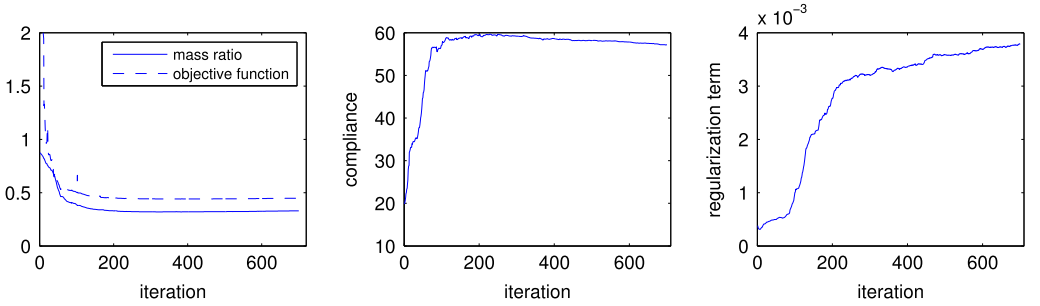

Fig. 25. Crack problem (model 2): convergence history for the mass ratio and objective function, the compliance and the regularization term for the final configuration shown in Fig. 23(e).

5. The velocity regularization techniques (logarithmic scaling and reaction term regularization) described in Section 3.2 and remarked in [35], were again crucial in the present work to avoid premature locking of the boundary movement.

Acknowledgments

The authors would like to thank the anonymous reviewers for a detailed reading and for useful comments that contributed to improve the quality of the manuscript. The authors also thank CAPES Foundation: grant n. 99999.007026/2014-05, Ministry of Education of Brazil, Brasília, DF 70040-020, Brazil, CNPq-Conselho Nacional de Desenvolvimento Científico e Tecnológico, Brazil: grant n. 160952/2011-5 and Lemann Foundation that provided financial support for this research.

Appendix. Derivative of the regularized objective functional $J_R(\phi)$

Let $\delta\phi$ be a direction of the admissible variations of ϕ. The derivative of $J_R(\phi)$ (expression (26)) in the direction $\delta\phi$ can be written as

$$\frac{dJ_R(\phi)}{d\phi}[\delta\phi] = \frac{dJ(\phi)}{d\phi}[\delta\phi] + \frac{d}{d\phi}\left(\int_D \frac{1}{2}\tau\,|\nabla\phi|^2\,dD\right)[\delta\phi]. \tag{A.1}$$

The derivative $dJ(\phi)/d\phi$ is calculated in Section 3.1. Since $|\nabla\phi|^2 = \nabla\phi\cdot\nabla\phi$, the derivative of the regularization term can be rewritten as

$$\frac{d}{d\phi}\left(\int_D \frac{1}{2}\tau\,|\nabla\phi|^2\,dD\right)[\delta\phi] = \int_D \tau\nabla\phi\cdot\nabla\left(\delta\phi\right)dD. \tag{A.2}$$

Using the equality

$$\nabla\phi\cdot\nabla\delta\phi = \mathrm{div}(\nabla\phi\,\delta\phi) - \Delta\phi\,\delta\phi, \tag{A.3}$$

(where Δ represents the Laplacian operator) and Divergence Theorem, we have

$$\frac{d}{d\phi}\left(\int_D \frac{1}{2}\tau\,|\nabla\phi|^2\,dD\right)[\delta\phi] = \int_{\partial D\setminus\partial D_N}\tau\delta\phi\,\nabla\phi\cdot\mathbf{n}d\partial D + \int_{\partial D_N}\tau\delta\phi\,\nabla\phi\cdot\mathbf{n}d\partial D - \int_D \tau\Delta\phi\,\delta\phi dD. \tag{A.4}$$

Assuming the boundary conditions

$$\begin{cases}\nabla\phi\cdot\mathbf{n} = \dfrac{\partial\phi}{\partial\mathbf{n}} = 0 & \text{on } \partial D\setminus\partial D_N,\\ \delta\phi = 0 & \text{on } \partial D_N,\end{cases} \tag{A.5}$$

Eq. (A.4) is simply given by

$$\frac{d}{d\phi}\left(\int_D \frac{1}{2}\tau\,|\nabla\phi|^2\,dD\right)[\delta\phi] = -\int_D \tau\Delta\phi\,\delta\phi dD. \tag{A.6}$$

Substituting (A.6) into (A.1), the distributional form is obtained as

$$\frac{dJ_R(\phi)}{d\phi}[\delta\phi] = \frac{dJ(\phi)}{d\phi}[\delta\phi] - \int_D \tau\Delta\phi\,\delta\phi dD, \tag{A.7}$$

or in the differential form as

$$\frac{dJ_R(\phi)}{d\phi} = \frac{dJ(\phi)}{d\phi} - \tau\Delta\phi. \tag{A.8}$$

References

[1] P. Duysinx, M.P. Bendsøe, Topology optimization of continuum structures with local stress constraints, Internat. J. Numer. Methods Engrg. 1478 (June 1997) (1998) 1453–1478.

[2] J.T. Pereira, E.A. Fancello, C.S. Barcellos, Topology optimization of continuum structures with material failure constraints, Struct. Multidiscip. Optim. 26 (2004) 50–66.

[3] E.A. Fancello, J.T. Pereira, Structural topology optimization considering material failure constraints and multiple load conditions, Latin Amer. J. Solid Struct. 1 (2003) 3–24.
[4] E.A. Fancello, Topology optimization for minimum mass design considering local failure constraints and contact boundary conditions, Struct. Multidiscip. Optim. 32 (2006) 229–240.
[5] C.E.M. Guilherme, J.S.O. Fonseca, Topology optimization of continuum structures with e-relaxed stress constraints, in: M. Alves, H.S. da Costa Mattos (Eds.), Mechanics of Solids in Brazil, ABCM, Rio de Janeiro, Brasil, 2007, pp. 239–250.
[6] J. París, F. Navarrina, I. Colominas, M. Casteleiro, Topology optimization of continuum structures with local and global stress constraints, Struct. Multidiscip. Optim. 39 (2009) 419–437.
[7] J. París, F. Navarrina, I. Colominas, M. Casteleiro, Block aggregation of stress constraints in topology optimization of structures, Adv. Eng. Softw. 41 (3) (2010) 433–441.
[8] C. Le, J. Norato, T. Bruns, C. Ha, D. Tortorelli, Stress-based topology optimization for continua, Struct. Multidiscip. Optim. 41 (4) (2010) 605–620.
[9] E. Lee, K.A. James, J.R.R.A. Martins, Stress-constrained topology optimization with design-dependent loading, Struct. Multidiscip. Optim. 46 (5) (2012) 647–661.
[10] S.J. Moon, G.H. Yoon, A newly developed qp-relaxation method for element connectivity parameterization to achieve stress-based topology optimization for geometrically nonlinear structures, Comput. Methods Appl. Mech. Engrg. 265 (2013) 226–241. http://dx.doi.org/10.1016/j.cma.2013.07.001.
[11] Y. Luo, M.Y. Wang, Z. Kang, An enhanced aggregation method for topology optimization with local stress constraints, Comput. Methods Appl. Mech. Engrg. 254 (2013) 31–41.
[12] E. Holmberg, B. Torstenfelt, A. Klarbring, Stress constrained topology optimization, Struct. Multidiscip. Optim. 48 (1) (2013) 33–47.
[13] Y. Luo, M. Zhou, M.Y. Wang, Z. Deng, Reliability based topology optimization for continuum structures with local failure constraints, Comput. Struct. 143 (2014) 73–84. http://dx.doi.org/10.1016/j.compstruc.2014.07.009.
[14] G. Cheng, X. Guo, ϵ-relaxed approach in structural topology optimization, Struct. Multidiscip. Optim. 13 (1997) 258–266.
[15] M. Bruggi, On an alternative approach to stress constraints relaxation in topology optimization, Struct. Multidiscip. Optim. 36 (2) (2008) 125–141.
[16] M. Bruggi, P. Venini, A mixed FEM approach to stress-constrained topology optimization, Internat. J. Numer. Methods Engrg. 73 (12) (2008) 1693–1714.
[17] M. Bruggi, P. Duysinx, Topology optimization for minimum weight with compliance and stress constraints, Struct. Multidiscip. Optim. 46 (3) (2012) 369–384. http://dx.doi.org/10.1007/s00158-012-0759-7.
[18] Y. Luo, Z. Kang, Topology optimization of continuum structures with Drucker–Prager yield stress constraints, Comput. Struct. 90–91 (2012) 65–75. http://dx.doi.org/10.1016/j.compstruc.2011.10.008.
[19] S. Amstutz, A. Novotny, E. Souza Neto, Topological derivative-based topology optimization of structures subject to Drucker–Prager stress constraints, Comput. Methods Appl. Mech. Engrg. 233–236 (2012) 123–136. http://dx.doi.org/10.1016/j.cma.2012.04.004.
[20] S.H. Jeong, D.-H. Choi, G.H. Yoon, Fatigue and static failure considerations using a topology optimization method, Appl. Math. Model. 39 (3–4) (2015) 1137–1162. http://dx.doi.org/10.1016/j.apm.2014.07.020.
[21] T. Belytschko, S.P. Xiao, C. Parimi, Topology optimization with implicit functions and regularization, Internat. J. Numer. Methods Engrg. 57 (8) (2003) 1177–1196. http://dx.doi.org/10.1002/nme.824.
[22] G. Allaire, F. Jouve, A.M. Toader, Structural optimization using sensitivity analysis and a level-set method, J. Comput. Phys. 194 (2004) 363–393.
[23] M.Y. Wang, X.M. Wang, D.M. Guo, A level set method for structural topology optimization, Comput. Methods Appl. Mech. Engrg. 192 (2003) 217–224.
[24] N.P. van Dijk, K. Maute, M. Langelaar, F. van Keulen, Level-set methods for structural topology optimization: a review, Struct. Multidiscip. Optim. 48 (3) (2013) 437–472. http://dx.doi.org/10.1007/s00158-013-0912-y.
[25] A.L. Gain, G.H. Paulino, A critical comparative assessment of differential equation-driven methods for structural topology optimization, Struct. Multidiscip. Optim. 48 (4) (2013) 685–710. http://dx.doi.org/10.1007/s00158-013-0935-4.
[26] L. Van Miegroet, P. Duysinx, Stress concentration minimization of 2D filets using X-FEM and level set description, Struct. Multidiscip. Optim. 33 (4–5) (2007) 425–438. http://dx.doi.org/10.1007/s00158-006-0091-1.
[27] G. Allaire, F. Jouve, Minimum stress optimal design with the level set method, Engineering Analysis with Boundary Elements 32 (2008) 909–918. http://dx.doi.org/10.1016/j.enganabound.2007.05.007.
[28] X. Guo, W.S. Zhang, M.Y. Wang, P. Wei, Stress-related topology optimization via level set approach, Comput. Methods Appl. Mech. Engrg. 200 (47–48) (2011) 3439–3452. http://dx.doi.org/10.1016/j.cma.2011.08.016.
[29] M.Y. Wang, L. Li, Shape equilibrium constraint: a strategy for stress-constrained structural topology optimization, Struct. Multidiscip. Optim. 47 (3) (2013) 335–352. http://dx.doi.org/10.1007/s00158-012-0846-9.
[30] W.S. Zhang, X. Guo, M. Wang, P. Wei, Optimal topology design of continuum structures with stress concentration alleviation via level set method, Internat. J. Numer. Methods Engrg. 93 (2013) 942–959.
[31] X. Guo, W. Zhang, W. Zhong, Stress-related topology optimization of continuum structures involving multi-phase materials, Comput. Methods Appl. Mech. Engrg. 268 (2014) 632–655. http://dx.doi.org/10.1016/j.cma.2013.10.003.
[32] M. Burger, R. Stainko, Phase-field relaxation of topology optimization with local stress constraints, SIAM J. Control Optim. 45 (4) (2006) 1447–1466.
[33] S.H. Jeong, G.H. Yoon, A. Takezawa, D.-H. Choi, Development of a novel phase-field method for local stress-based shape and topology optimization, Comput. Struct. 132 (2014) 84–98. http://dx.doi.org/10.1016/j.compstruc.2013.11.004.
[34] S. Amstutz, A.A. Novotny, Topological optimization of structures subject to Von Mises stress constraints, Struct. Multidiscip. Optim. 41 (3) (2010) 407–420.
[35] H. Emmendoerfer Jr., E.A. Fancello, A level set approach for topology optimization with local stress constraints, Internat. J. Numer. Methods Engrg. 99 (April) (2014) 129–156. http://dx.doi.org/10.1002/nme.4676.

[36] J.A. Sethian, Level Set Method and Fast Marching Methods: Evolving Interfaces in Computational Geometry, Fluid Mechanics, Computer Vision, and Materials Science, Cambridge University Press, Cambridge, U.K, 1999.
[37] S.Y. Wang, K.M. Lim, B.C. Khoo, M.Y. Wang, An extended level set method for shape and topology optimization, J. Comput. Phys. 221 (2007) 395–421.
[38] H. Jia, H. Beom, Y. Wang, S. Lin, B. Liu, Evolutionary level set method for structural topology optimization, Comput. Struct. 89 (2011) 445–454.
[39] P.D. Dunning, H.A. Kim, A new hole insertion method for level set based structural topology optimization, Internat. J. Numer. Methods Engrg. 93 (2013) 118–134. http://dx.doi.org/10.1002/nme.
[40] T. Yamada, K. Izui, S. Nishiwaki, A. Takezawa, A topology optimization method based on the level set method incorporating a fictitious interface energy, Comput. Methods Appl. Mech. Engrg. 199 (45–48) (2010) 2876–2891.
[41] J.S. Choi, T. Yamada, K. Izui, S. Nishiwaki, J. Yoo, Topology optimization using a reaction–diffusion equation, Comput. Methods Appl. Mech. Engrg. 200 (29–32) (2011) 2407–2420. http://dx.doi.org/10.1016/j.cma.2011.04.013.
[42] S. Osher, J. Sethian, Fronts propagating with curvature-dependent speed: Algorithms based on Hamilton–Jacobi formulations, J. Comput. Phys. 79 (1988) 12–49.
[43] N.P.V. Dijk, M. Langelaar, F.V. Keulen, Explicit level-set-based topology optimization using an exact heaviside function and consistent sensitivity analysis, Internat. J. Numer. Methods Engrg. 91 (May) (2012) 67–97.
[44] Q. Xia, T. Shi, S. Liu, M.Y. Wang, A level set solution to the stress-based structural shape and topology optimization, Comput. Struct. 90–91 (2012) 55–64.
[45] D.P. Bertsekas, Constrained Optimization and Lagrange Multiplier Methods, Athena Scientific, Belmont, MA, U.S.A, 1996.
[46] J.M. Martínez, Otimização prática usando o Lagrangiano Aumentado, Tech. Rep, IMECC-UNICAMP, 2009.
[47] S. Osher, R. Fedkiw, Level Set Methods and Dynamic Implicit Surfaces, Vol. 57, Springer, New York, 2003.
[48] F. Gournay, Velocity extension for the level-set method and multiple eigenvalues in shape optimization, SIAM J. Control Optim. 45 (1) (2006) 343–367.